Article

Imaging surface structure and premelting of ice Ih with atomic resolution

https://doi.org/10.1038/s41586-024-07427-8

Received: 18 August 2023

Accepted: 16 April 2024

Published online: 22 May 2024

Check for updates

Jiani Hong[1,11], Ye Tian[1,11]✉, Tiancheng Liang[1,11], Xinmeng Liu[1,11], Yizhi Song[1], Dong Guan[1], Zixiang Yan[1], Jiadong Guo[1], Binze Tang[1], Duanyun Cao[2,3], Jing Guo[4], Ji Chen[5,6], Ding Pan[7], Li-Mei Xu[1,6,8]✉, En-Ge Wang[1,6,8,9]✉ & Ying Jiang[1,6,8,10]✉

Ice surfaces are closely relevant to many physical and chemical properties, such as melting, freezing, friction, gas uptake and atmospheric reaction[1–8]. Despite extensive experimental and theoretical investigations[9–17], the exact atomic structures of ice interfaces remain elusive owing to the vulnerable hydrogen-bonding network and the complicated premelting process. Here we realize atomic-resolution imaging of the basal (0001) surface structure of hexagonal water ice (ice Ih) by using qPlus-based cryogenic atomic force microscopy with a carbon monoxide-functionalized tip. We find that the crystalline ice-Ih surface consists of mixed Ih- and cubic (Ic)-stacking nanodomains, forming $\sqrt{19} \times \sqrt{19}$ periodic superstructures. Density functional theory reveals that this reconstructed surface is stabilized over the ideal ice surface mainly by minimizing the electrostatic repulsion between dangling OH bonds. Moreover, we observe that the ice surface gradually becomes disordered with increasing temperature (above 120 Kelvin), indicating the onset of the premelting process. The surface premelting occurs from the defective boundaries between the Ih and Ic domains and can be promoted by the formation of a planar local structure. These results put an end to the longstanding debate on ice surface structures and shed light on the molecular origin of ice premelting, which may lead to a paradigm shift in the understanding of ice physics and chemistry.

In the conventional view, the crystalline ice surface is simply considered as a truncated plane from the bulk without any reconstruction[11,18]. However, it is commonly known that the atoms on solid surfaces tend to rearrange to minimize the surface energy. Whether a similar reconstruction is present on the ice surface and what the proton order is still remain elusive. In addition, the ice surface can melt even well below the bulk melting temperature, corresponding to the so-called premelting process that has been under longstanding debate[1]. Only based on a clear microscopic understanding of the nature of the most stable ice surface can one further explore the origin and mechanism of surface premelting.

The structures of bulk ices with different phases have been well determined by crystallographic methods[19–21]. By contrast, probing ice surfaces is much more demanding, and mainly relies on surface-sensitive diffraction and spectroscopic techniques, such as low-energy electron diffraction[18], helium-atom scattering[11,22], X-ray absorption spectroscopy[23] and sum frequency generation spectroscopy[12,24–27]. Even if there is some indication that the outermost surface layer differs from the bulk structure, these methods cannot resolve the nanoscale or atomic inhomogeneity of the ice surface and premelting structures because of poor spatial resolution and spatially averaged effects (Methods and Supplementary Table 1).

Although high-resolution scanning tunnelling microscopy (STM) can be used to determine the morphology and structure of few-layer ice films[13,28,29], the bulk ice is not accessible to STM owing to its insulating nature. Non-contact atomic force microscopy (AFM) has been also applied to probe the ice surface in real space[17,30]. However, it is challenging to achieve atomic resolution on the ice surface owing to the disturbance of the tip on the fragile hydrogen (H)-bonding structure and the difficulty of accessing the short-range force region. It has been suggested that dangling OH bonds on the ice surface might be short-range reconstructed[14,17,31], but the detailed topology of the H-bonding network on the ice surface is yet to be determined.

In recent years, the weakly perturbative qPlus-AFM technique with a carbon monoxide (CO)-functionalized tip[32–34] has been proven successful for probing low-dimensional water/ice structures on conductive surfaces with atomic resolution[35–37], while its application to completely insulating multilayer ices or bulk ices is highly non-trivial. In this work,

[1]International Center for Quantum Materials, School of Physics, Peking University, Beijing, People's Republic of China. [2]Beijing Key Laboratory of Environmental Science and Engineering, School of Materials Science and Engineering, Beijing Institute of Technology, Beijing, People's Republic of China. [3]Beijing Institute of Technology Chongqing Innovation Center, Chongqing, People's Republic of China. [4]College of Chemistry, Beijing Normal University, Beijing, People's Republic of China. [5]School of Physics, Peking University, Beijing, People's Republic of China. [6]Interdisciplinary Institute of Light-Element Quantum Materials and Research Center for Light-Element Advanced Materials, Peking University, Beijing, People's Republic of China. [7]Department of Physics and Department of Chemistry, The Hong Kong University of Science and Technology, Hong Kong, People's Republic of China. [8]Collaborative Innovation Center of Quantum Matter, Beijing, People's Republic of China. [9]Tsientang Institute for Advanced Study, Zhejiang, People's Republic of China. [10]New Cornerstone Science Laboratory, Peking University, Beijing, People's Republic of China. [11]These authors contributed equally: Jiani Hong, Ye Tian, Tiancheng Liang, Xinmeng Liu. ✉e-mail: tianye420@pku.edu.cn; limei.xu@pku.edu.cn; egwang@pku.edu.cn; yjiang@pku.edu.cn

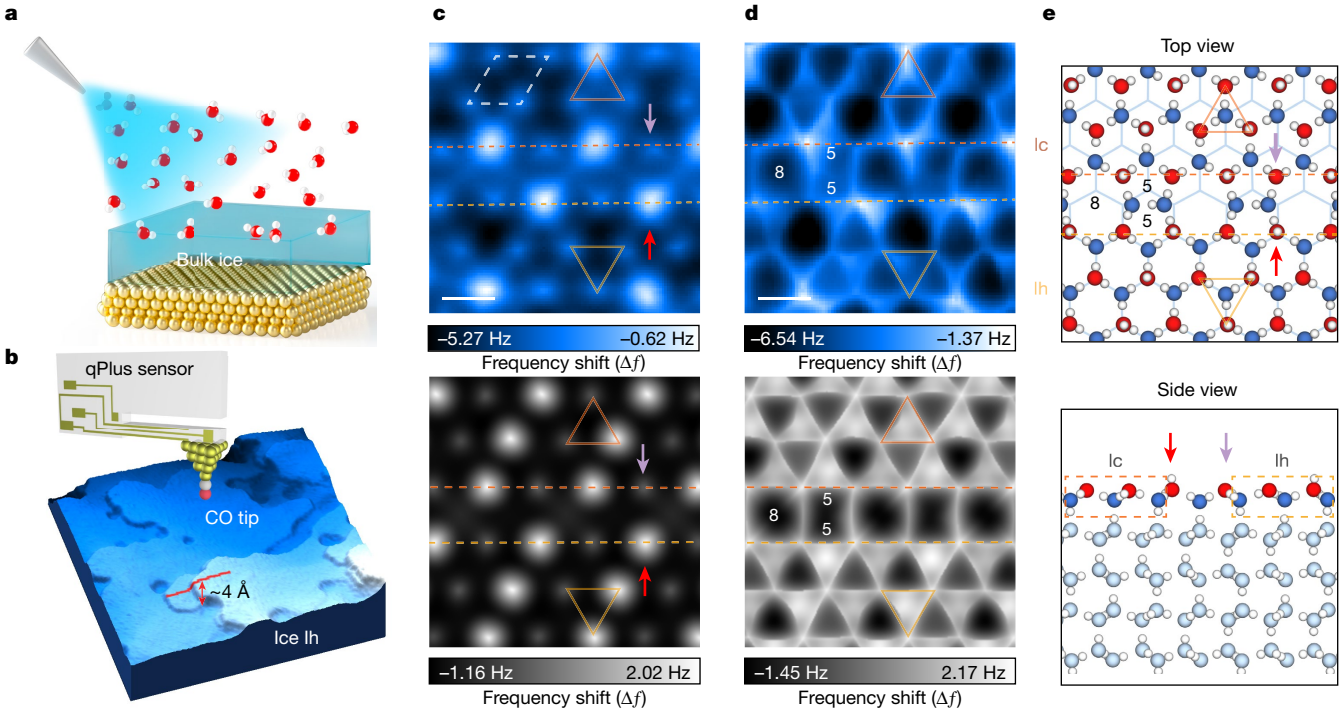

Fig. 1 | Boundary structure between Ih- and Ic-stacking domains on the (0001) surface of hexagonal ice. a, Schematic diagram of the bulk ice-Ih growth process. Water vapour was deposited onto the cold metal surface under vacuum. Thick and uniform ice films formed after a long-time deposition. **b**, Schematic of AFM imaging of the ice surface (grown at 133 K) by using qPlus-AFM with a CO-functionalized tip. The constant-frequency-shift AFM image shows the overall surface morphology of ice Ih, at the set point of −1.8 Hz. The line profile across the step edge shows the height of an ice bilayer (about 4 Å). **c**,**d**, Constant-height AFM images (top) and simulations (bottom) of in-plane stacking disorder at the ice surface (grown at 133 K), obtained at tip heights of −100 pm (top) and 23.8 Å (bottom) (**c**) and −200 pm (top) and 22.7 Å (bottom) (**d**). The unit cell is denoted by a white dashed rhombus in **c**. Scale bars, 5 Å. **e**, Top and side views of the ice-Ih (0001) surface. The side view corresponds to the second prism face ($10\bar{2}0$). H atoms are denoted as white spheres. O atoms in the upper-lying and lower-lying water molecules in the topmost bilayer and in the bulk are denoted as red, dark blue and light blue spheres, respectively. For clarity, bilayers below the surface are shown in light blue in the top view. H-up and O-up water molecules are denoted by red and purple arrows, respectively, and single-tetrahedron Ic and Ih structures are denoted by orange and yellow triangles, respectively. The orange and yellow dashed lines represent the boundary between Ic and Ih domains, consisting of 55–8-membered rings.

we advance the qPlus-AFM technique to directly image the surface of hexagonal water ice (ice Ih), the most abundant ice form in nature (Methods). By combining the force imaging of high-order electrostatics and Pauli repulsion, the molecular orientation and local tetrahedral structure of water are unambiguously distinguished, which allows us to determine the reconstruction of the most stable basal (0001) surface and the initial premelting process with increasing temperature.

The crystalline ice-Ih films were grown on Au(111) or Pt(111) substrates through water vapour deposition at low temperatures under vacuum conditions (Methods, Fig. 1a and Supplementary Fig. 1). These ice films are thick enough (larger than 250 nm) such that they can be considered as substrate-independent bulk ice Ih with the (0001) plane exposed. The constant-frequency-shift AFM image shows the overall morphology of the ice-Ih surface (Methods and Fig. 1b). The measured surface step height is around 4 Å, in accordance with a bilayer for the basal face of ice Ih. Owing to the local tetrahedral H-bonding configuration of water molecules, the ice Ih is composed of puckered hexagonal bilayers. The formation of the ice-Ih phase on both substrates was confirmed by the presence of double spirals created typically by screw dislocations with a double Burgers vector[30] (Supplementary Fig. 2).

To identify the atomic structure of the ice surface, we performed systematic constant-height AFM imaging at different tip heights, as well as AFM simulations based on density functional theory (DFT) calculations (Fig. 1c,d and Supplementary Fig. 3). In the upper part of the topmost ice bilayer, the water molecules are three-coordinated and have two orientations: H-up and O-up (highlighted by red and purple arrows in Fig. 1e). At a large tip height, the H-up water molecules are visualized as individual depressions with random distribution, mainly arising from the higher-order electrostatic attraction force between the CO tip and the H atoms of water[34] (Extended Data Fig. 1). When the tip approaches the surface, the H-up water molecules evolve into bright protrusions and the O-up water molecules are resolved with less brightness (Fig. 1c). When the tip height is further decreased so that the Pauli repulsive force dominates, solid triangular structures are clearly visualized (Fig. 1d), corresponding to three upper-lying water molecules bonded to one lower-lying water molecule in tetrahedral configuration (Fig. 1e).

The tetrahedron structures have two orientations rotated by 180° (Fig. 1d), suggesting different layer stacking. The O atoms of water molecules in the topmost bilayer for Ih-stacking is a mirror image of those in the underlying bilayer, whereas for cubic (Ic)-stacking, the outermost bilayer shifts with regard to the underlying bilayer in a diamond-structure arrangement[19] (side view in Fig. 1e). In contrast to the inter-bilayer stacking-disordered ice[38], here the Ih domains are interlaced with Ic domains in the nanoscale at the ice surface, leading to an intra-bilayer stacking disorder (see dashed lines in Fig. 1c,d). The DFT calculations reveal that the formation energies of an Ih- or Ic-stacking surface bilayer on the Ih substrate are similar (Supplementary Fig. 4). The boundaries between Ih and Ic domains consist of a coupled five- and eight-membered rings (55–8) line defect (top view in Fig. 1e), which can be clearly discerned in high-resolution AFM images (Fig. 1c,d and Supplementary Fig. 3). Molecular-dynamics simulations

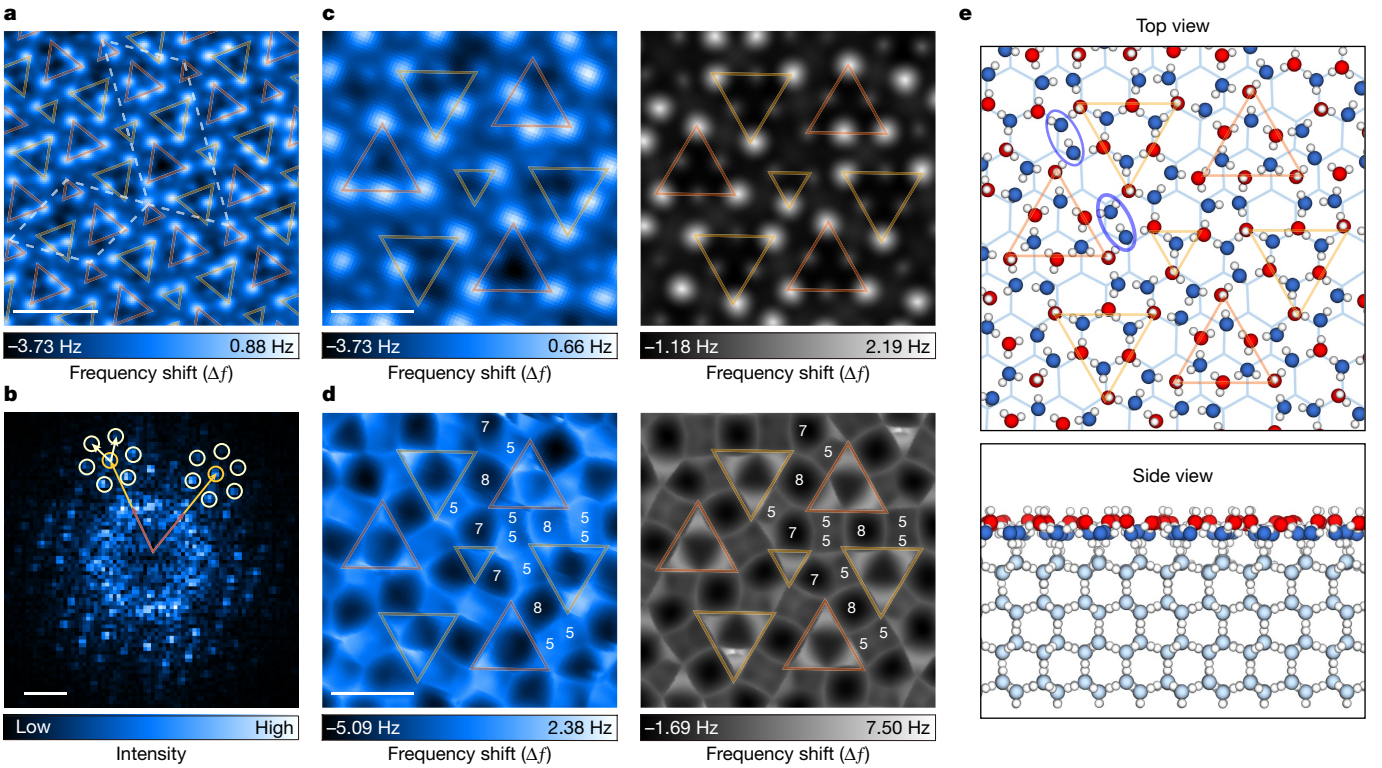

Fig. 2 | Periodic superstructures at the reconstructed ice surface. a,**b**, The constant-height AFM image (**a**) and the corresponding FFT image (**b**) of the superstructure (grown at 120 K). The $\sqrt{19} \times \sqrt{19}$ and $2\sqrt{19} \times \sqrt{19}$ unit cells are indicated by the dashed white rhombuses. The 1 × 1 spots and their satellite spots are denoted by yellow and white circles, respectively. The reciprocal vectors of the 1 × 1 surface, superstructure and the central hexagon are indicated by yellow, white and red arrows, respectively. **c**,**d**, Zoom-in constant-height AFM images (left) and the simulations (right) of the pinwheel-like structure in the $2\sqrt{19} \times \sqrt{19}$ phase, at tip heights of −240 pm and 23.50 Å (**c**) and −330 pm and 22.10 Å (**d**), respectively. Three types of defective boundary (57–8–57, 55–8–55 and 55–8–57) are marked in the images. **e**, Top and side views of the calculated configurations of the pinwheel-like structure. The single-tetrahedron structure is surrounded by six triple-tetrahedron structures. The orange and yellow triangles represent tetrahedron structures in different stacking types. Dimers consisting of two lower-lying water molecules are indicated by blue circles. H atoms and O atoms in the upper-lying and lower-lying water molecules in the topmost bilayer are denoted as white, red and dark blue spheres, respectively. Bilayers below the surface are shown in light blue. Scale bars, 2 nm (**a**), 1 nm^{-1} (**b**), 1 nm (**c**,**d**).

of water vapour deposition on an ice-Ih surface (Methods) show that such an intra-bilayer stacking disorder exists on only the topmost surface (Extended Data Fig. 2 and Supplementary Video 1), which is consistent with our AFM observation that the Ic and Ih domains have perfect periodicity and are atomically flat.

We found that the sizes of Ih and Ic nanodomains are temperature dependent. Around 120 K, well-ordered superstructures are formed by Ih and Ic nanodomains with two characteristic sizes: triple tetrahedron and single tetrahedron (see solid triangles in Fig. 2a and Supplementary Fig. 5). The superstructures have two periodicities: $\sqrt{19} \times \sqrt{19} - R23.41°$ and $2\sqrt{19} \times \sqrt{19} - R23.41°$ (Wood's notation, in which R represents the rotation angle; see dashed rhombuses in Fig. 2a, left), showing long-range ordering (Extended Data Fig. 3). The corresponding fast Fourier transform (FFT) image (Fig. 2b) reveals the 1 × 1 spots (yellow circles) accompanied by distinct six-fold satellite spots (white circles), aligning with the $\sqrt{19} \times \sqrt{19}$ periodicity. In addition, a broadened hexagonal pattern is observed (Fig. 2b and Supplementary Fig. 6), reflecting a short-range 2.1 × 2.1 order of dangling OH bonds at Ih and Ic boundaries (see red arrows in Fig. 2b and Methods). This result provides atomic insight into the origin of the weak 2.1 × 2.1 diffraction pattern observed in the previous helium-atom scattering experiment[22], which is slightly larger than the proposed ×2 order at the ideal 1 × 1 ice surface[14]. The $\sqrt{19} \times \sqrt{19}$ phase occurs if all the single-tetrahedron structures are in the same stacking type. When the single-tetrahedron structures with two stacking types are aligned in a stripe pattern, a $2\sqrt{19} \times \sqrt{19}$ lattice forms. The zoom-in AFM images show a pinwheel-like structure, which consists of a single-tetrahedron structure surrounded by six triple-tetrahedron structures arranged alternatively with Ih and Ic stacking (see yellow and orange triangles in Fig. 2c,d). For the $2\sqrt{19} \times \sqrt{19}$ phase, there are three types of defective boundary, 55–8–55, 57–8–57 and 55–8–57 line defects, whereas there is only the 55–8–57 line defect for the $\sqrt{19} \times \sqrt{19}$ phase (Extended Data Fig. 4).

To explore the stability of surface superstructures, we performed detailed DFT-based energetic calculations (Fig. 3). Under any specific pattern of water molecules adopted at the surface, not only the number of H-up water molecules (dangling OH bonds) but also their ordering has an important role in the surface energy of ice[39]. We constructed two periodic structures ($\sqrt{19} \times \sqrt{19}$ and $2\sqrt{19} \times \sqrt{19}$) with a ratio of 7:8 between the H-up and O-up water molecules, which is closest to the value observed in the experiment (1:1.14). The order parameter S_{OH} is defined as the total number of nearest-neighbour dangling OH pairs (Methods and Extended Data Figs. 5 and 6). Similar to a previous study[39], the value of S_{OH} quantifies the average separation between the dangling OH bonds at the surface: a smaller S_{OH} corresponds to a more homogeneous distribution of dangling OH bonds, leading to smaller electrostatic repulsion.

We calculated multiple structures with different S_{OH} in $\sqrt{19} \times \sqrt{19}$, $2\sqrt{19} \times \sqrt{19}$ and 1 × 1 surfaces and compared their formation energy per water molecule in the topmost bilayer with different S_{OH} (Fig. 3). The electrostatic repulsion within each pair of nearest-neighbour dangling OH bonds contributes to the increase in formation energy (Supplementary Fig. 7), resulting in a positive linear relation between S_{OH}

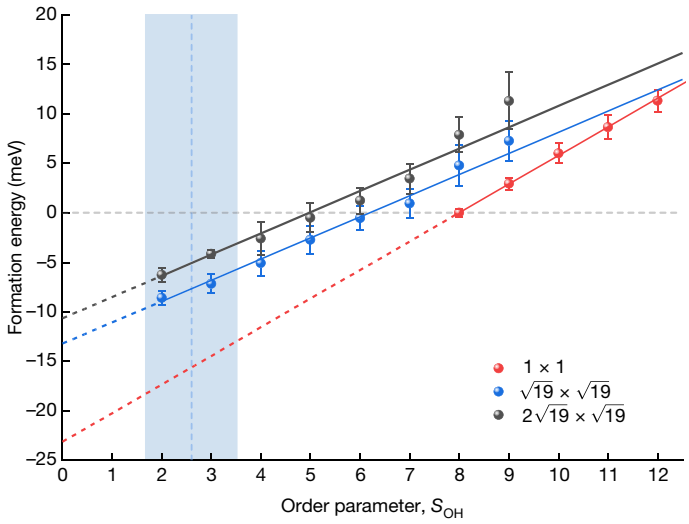

Fig. 3 | Formation energies of different ice surface phases as a function of order parameter S_{OH}. Formation energies per water molecule in the topmost bilayer versus order parameter S_{OH} are derived by DFT-based energetic calculations. To facilitate direct comparison, the zero energy is set to be the minimum formation energy of the ideal 1 × 1 surface, corresponding to $S_{OH} = 8$. A linear correlation between formation energy and S_{OH} can be obtained on $\sqrt{19} \times \sqrt{19}$, $2\sqrt{19} \times \sqrt{19}$ and 1 × 1 surfaces, owing to the repulsive interaction energy of two nearest-neighbouring dangling OH bonds. The S_{OH} starts from the theoretical minimum value, $S_{OH} = 2$ for the two superstructures and $S_{OH} = 8$ for the ideal surface. For $\sqrt{19} \times \sqrt{19}$ and 1 × 1 phases, data points for each S_{OH} value represent the averaged formation energy calculated for eight surface structures with different H-bonding configurations and error bars represent their standard deviation. For the $2\sqrt{19} \times \sqrt{19}$ phase, only three surface structures at each S_{OH} were calculated owing to the need for much larger amount of computation with the bigger unit cell. The dashed vertical line and shaded blue area represent the average $S_{OH} = 2.6$ and the standard deviation for superstructures obtained in experiment, respectively. The Ih substrate remains consistent in all phases, with an S_{OH} value of 11.

and formation energy. We found that the superstructures with homogeneous arrangements of dangling OH bonds ($S_{OH} \leq 5$) are generally stabilized over the ideal 1 × 1 surface. We note that the average S_{OH} for superstructures in experiments is 2.6 (see the blue dashed line in Fig. 3 and Extended Data Fig. 5), close to the most stable configuration in simulations. Moreover, the coexistence of $\sqrt{19} \times \sqrt{19}$ and $2\sqrt{19} \times \sqrt{19}$ phases could be attributed to the tiny difference in their formation energies. The entropy contribution to surface stability, which arises from the presence of defective boundaries, is estimated to be a minor factor considering the local order of protons and the long-range order of oxygen lattice. In addition, the stability of the superstructures is further confirmed through molecular-dynamics simulations at 120 K, using different water models (Methods).

Disregarding any electrostatic repulsion between dangling OH bonds ($S_{OH} = 0$), the formation energy of the ideal surface is around 10 meV per water molecule smaller than the superstructures (see the dashed extrapolation line in Fig. 3). Such an energy loss in the superstructures results from the formation of five-, seven- and eight-membered rings at defective boundaries. However, the formation energy shows a strong dependence on S_{OH} at the surface. The increase of formation energy due to the electrostatic contribution is much smaller in the superstructures (with the smallest possible S_{OH} of 2) than that of the ideal surface (with the smallest possible S_{OH} of 8, including the 2 × 1 stripe order[14]), thus stabilizing the superstructures over the ideal 1 × 1 surface by about 10 meV per water molecule. The calculation of surface energy could yield the same conclusion (Methods and Extended Data Fig. 7). Therefore, minimizing the electrostatic repulsion between dangling OHs is the main driving force for the surface reconstruction of ice Ih.

We emphasize that the reduced electrostatic energy of superstructures is closely related to its special H-bonding topology. For clarity, we take the $\sqrt{19} \times \sqrt{19}$ superstructure as an example, which contains 15 upper-lying undercoordinated and 19 lower-lying fully coordinated water molecules in each unit cell. By contrast, the ideal surface of the same area has 19 water molecules in both the upper and lower layers. The reconstructed ice surface has four fewer undercoordinated water molecules due to the H-bond formation between the lower-lying water molecules in five- and seven-membered rings. The lower-lying water pairs (blue circles in Fig. 2) separate the ice surface into tiny Ic and Ih nanodomains, thus effectively decreasing the nearest-neighbour sites of each undercoordinated water molecule within the topmost bilayer. Such a H-bonding topology can significantly reduce the number of dangling OH pairs (S_{OH}: from 8 to 2) and weaken the S_{OH} dependence of the formation energy (see the slope change in Fig. 3). We note that the stacking-fault reconstruction on the ice surface is analogous to other tetrahedrally bonded crystals, such as the 7 × 7 reconstruction of Si(111) surface[40]. However, the underlying mechanism for energetic optimization is completely different. For the latter, the driving force is simply the saturation of dangling covalent bonds.

To further study the premelting behaviour of the ice surface, we grew the ice samples at temperatures higher than that for the periodic superstructure phase (>120 K). At 123 K, Ic and Ih domains of different sizes emerge sporadically within the superstructure phase, leading to local disordering (highlighted by red arrows in Fig. 4a and Supplementary Fig. 8). With further increasing the growth temperature (>125 K), the superstructures disappear completely (Fig. 4b), and planar local structures (PLSs) are observed at the boundary between unevenly sized Ic and Ih domains (highlighted by red dashed ellipses in Fig. 4b). The corresponding FFT image reveals significantly broadened 1 × 1 spots and a homogeneous ×2 ring structure (Supplementary Fig. 6). The detailed atomic structure of the PLS could be derived from a metastable precursor, which is formed occasionally by adding one interstitial water molecule into the eight-membered ring (Fig. 4c,d). On the basis this precursor, the lower-lying water molecule in the bilayer lifts up (highlighted by green arrows in Fig. 4e), forming a nearly planar structure together with two higher-lying and the interstitial water molecules. In experiment, the PLS is the most common metastable structure on the premelted ice surfaces whereas the non-planar local structure was rarely observed, showing the higher stability of the PLS (Supplementary Fig. 9).

The formation of the PLS is accompanied by complicated rearrangement of inter- and intralayer H-bonding networks. Owing to the highly complex nature of the disordered surroundings of the PLS (Extended Data Figs. 8 and 9), here we propose one possible pathway based on the relatively simple local environment (Fig. 4c–e). A higher-lying water molecule originally located at an Ic-stacking site of top bilayer moves to an Ih-stacking site (highlighted by red arrows in Fig. 4d,e). Meanwhile, the nearby lower-lying water molecule (highlighted by green arrows in Fig. 4d,e) lifts up to the upper part of the top bilayer. The water molecule (highlighted by blue arrows in Fig. 4d,e), originally located in the second topmost bilayer, breaks the bond with the nearby water molecules and accordingly moves upwards to the surface, forming a H bond with the PLS and leaving a vacancy in the second topmost bilayer (Supplementary Fig. 10). The formation of PLS may widen the Ih and Ic boundaries and induce large-scale surface disorder in its surrounding region (see the white dashed region in Fig. 4b). In addition, the PLS could rotate, which further increases the degree of surface disorder (Supplementary Fig. 11). A decrease in the number of dangling OH bonds was observed with increasing the temperature (Supplementary Fig. 12), consistent with previous sum frequency generation results[25] (Methods).

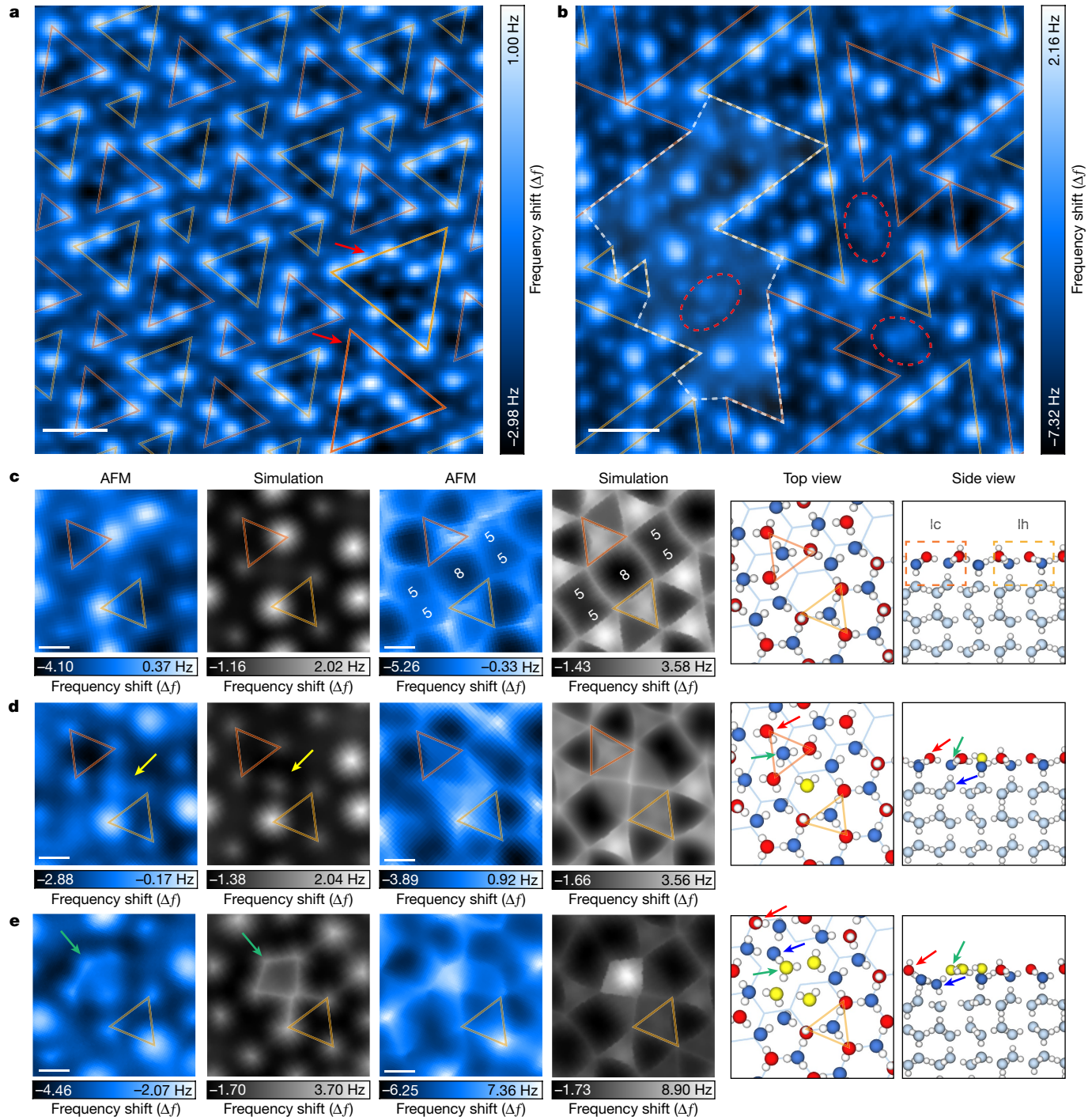

Fig. 4 | The onset of ice surface premelting. a,**b**, Constant-height AFM images showing the initial disordering (red arrows) in superstructures (grown at 123 K; **a**) and the coexistence of larger-scale surface disorder and PLSs (grown at 125 K; **b**). The PLSs and the peripheries of the Ic and Ih domains are indicated by red dashed ellipses and orange and yellow lines, respectively. The structures deviating from the tetrahedral configuration are regarded as surface disorder, indicated by white dashed lines. **c**, Atomic structure of the 55–8–55 boundary between Ih and Ic domains. **d**, Atomic structure of the PLS precursor. The additional water molecule in the eight-membered ring is indicated by yellow arrows in the AFM and simulation images, and its O atom is denoted as yellow spheres in the schematic models. **e**, Atomic structure of the PLS. The O atoms of the PLS are denoted as yellow spheres in the schematic models. The water molecule that lifts up to the upper part of the surface bilayer is indicated by green arrows. Water molecules involved in inter- and intralayer H-bonding adjustments are shown by blue and red arrows, respectively. Tip heights for **c**–**e** (from left to right): −100 pm and 23.80 Å, −180 pm and 22.60 Å (**c**); −100 pm and 23.80 Å, −260 pm and 22.70 Å (**d**); −100 pm and 23.30 Å, −160 pm and 22.70 Å (**e**). Different stacking types at the surface are highlighted by orange and yellow triangles. The O atoms of the upper-lying and lower-lying water molecules in the topmost bilayer are denoted as red and blue spheres in schematic models, respectively. Bilayers below the surface are shown in light blue. Scale bars, 1 nm (**a**,**b**), 3 Å (**c**–**e**).

Those results could be regarded as the onset of surface premelting (Extended Data Fig. 9), where the PLSs at the defective Ih and Ic boundaries serve as local seeds. Our work directly visualizes the detailed structural order–disorder transition on the ice surface, which provides a different molecular perspective on the origin and mechanism of premelting. The intrinsic existence of defective Ih and

Ic boundaries and the PLSs on the ice surface may have indispensable roles in the phase transition, adsorption, surface reaction, and ice nucleation and growth. In addition, the knowledge obtained from this work could also be useful for understanding the formation and structure of the quasi-liquid layer on ice surfaces, which provides an opportunity for future exploration of the detailed phase diagram of ice surfaces.

Online content

Any methods, additional references, Nature Portfolio reporting summaries, source data, extended data, supplementary information, acknowledgements, peer review information; details of author contributions and competing interests; and statements of data and code availability are available at https://doi.org/10.1038/s41586-024-07427-8.

1. Slater, B. & Michaelides, A. Surface premelting of water ice. *Nat. Rev. Chem.* **3**, 172–188 (2019).
2. Jia, Z. C., DeLuca, C. I., Chao, H. M. & Davies, P. L. Structural basis for the binding of a globular antifreeze protein to ice. *Nature* **384**, 285–288 (1996).
3. Matsumoto, M., Saito, S. & Ohmine, I. Molecular dynamics simulation of the ice nucleation and growth process leading to water freezing. *Nature* **416**, 409–413 (2002).
4. Canale, L. et al. Nanorheology of interfacial water during ice gliding. *Phys. Rev. X* **9**, 041025 (2019).
5. Devlin, J. P., Uras, N., Sadlej, J. & Buch, V. Discrete stages in the solvation and ionization of hydrogen chloride adsorbed on ice particles. *Nature* **417**, 269–271 (2002).
6. Huthwelker, T., Ammann, M. & Peter, T. The uptake of acidic gases on ice. *Chem. Rev.* **106**, 1375–1444 (2006).
7. Molina, M. J., Tso, T. L., Molina, L. T. & Wang, F. C. Y. Antarctic stratospheric chemistry of chlorine nitrate, hydrogen-chloride and ice release of active chlorine. *Science* **238**, 1253–1257 (1987).
8. Hama, T. & Watanabe, N. Surface processes on interstellar amorphous solid water: adsorption, diffusion, tunneling reactions, and nuclear-spin conversion. *Chem. Rev.* **113**, 8783–8839 (2013).
9. Kiselev, A. et al. Active sites in heterogeneous ice nucleation-the example of K-rich feldspars. *Science* **355**, 367–371 (2017).
10. Moore, E. B. & Molinero, V. Structural transformation in supercooled water controls the crystallization rate of ice. *Nature* **479**, 506–508 (2011).
11. Braun, J., Glebov, A., Graham, A. P., Menzel, A. & Toennies, J. P. Structure and phonons of the ice surface. *Phys. Rev. Lett.* **80**, 2638–2641 (1998).
12. Wei, X., Miranda, P. B. & Shen, Y. R. Surface vibrational spectroscopic study of surface melting of ice. *Phys. Rev. Lett.* **86**, 1554–1557 (2001).
13. Mehlhorn, M. & Morgenstern, K. Faceting during the transformation of amorphous to crystalline ice. *Phys. Rev. Lett.* **99**, 246101 (2007).
14. Buch, V., Groenzin, H., Lit, I., Shultz, M. J. & Tosatti, E. Proton order in the ice crystal surface. *Proc. Natl Acad. Sci. USA* **105**, 5969–5974 (2008).
15. Watkins, M. et al. Large variation of vacancy formation energies in the surface of crystalline ice. *Nat. Mater.* **10**, 794–798 (2011).
16. Asakawa, H., Sazaki, G., Nagashima, K., Nakatsubo, S. & Furukawa, Y. Two types of quasi-liquid layers on ice crystals are formed kinetically. *Proc. Natl Acad. Sci. USA* **113**, 1749–1753 (2016).
17. Kawakami, N., Iwata, K., Shiotari, A. & Sugimoto, Y. Intrinsic reconstruction of ice-I surfaces. *Sci. Adv.* **6**, eabb7986 (2020).
18. Materer, N. et al. Molecular surface structure of a low-temperature ice Ih(0001) crystal. *J. Phys. Chem.* **99**, 6267–6269 (1995).
19. Hobbs, P. V. *Ice Physics* (OUP, 2010).
20. Huang, X. et al. Tracking cubic ice at molecular resolution. *Nature* **617**, 86–91 (2023).
21. Rosu-Finsen, A. et al. Medium-density amorphous ice. *Science* **379**, 474–478 (2023).
22. Glebov, A., Graham, A. P., Menzel, A., Toennies, J. P. & Senet, P. A helium atom scattering study of the structure and phonon dynamics of the ice surface. *J. Chem. Phys.* **112**, 11011–11022 (2000).
23. Nordlund, D. et al. Surface structure of thin ice films. *Chem. Phys. Lett.* **395**, 161–165 (2004).
24. Sánchez, M. A. et al. Experimental and theoretical evidence for bilayer-by-bilayer surface melting of crystalline ice. *Proc. Natl Acad. Sci. USA* **114**, 227–232 (2016).
25. Sugimoto, T. et al. Topologically disordered mesophase at the topmost surface layer of crystalline ice between 120 and 200 K. *Phys. Rev. B* **99**, 121402 (2019).
26. Smit, W. J. et al. Excess hydrogen bond at the ice-vapor interface around 200 K. *Phys. Rev. Lett.* **119**, 133003 (2017).
27. Nojima, Y., Suzuki, Y., Takahashi, M. & Yamaguchi, S. Proton order toward the surface of ice Ih revealed by heterodyne-detected sum frequency generation spectroscopy. *J. Phys. Chem. Lett.* **8**, 5031–5034 (2017).
28. Thürmer, K. & Bartelt, N. C. Growth of multilayer ice films and the formation of cubic ice imaged with STM. *Phys. Rev. B* **77**, 195425 (2008).
29. Maier, S., Lechner, B. A. J., Somorjai, G. A. & Salmeron, M. Growth and structure of the first layers of ice on Ru(0001) and Pt(111). *J. Am. Chem. Soc.* **138**, 3145–3151 (2016).
30. Thürmer, K. & Nie, S. Formation of hexagonal and cubic ice during low-temperature growth. *Proc. Natl Acad. Sci. USA* **110**, 11757–11762 (2013).
31. Fletcher, N. H. Reconstruction of ice crystal surfaces at low temperatures. *Phil. Mag. B* **66**, 109–115 (1992).
32. Giessibl, F. J. Advances in atomic force microscopy. *Rev. Mod. Phys.* **75**, 949–983 (2003).
33. Gross, L., Mohn, F., Moll, N., Liljeroth, P. & Meyer, G. The chemical structure of a molecule resolved by atomic force microscopy. *Science* **325**, 1110–1114 (2009).
34. Peng, J. et al. Weakly perturbative imaging of interfacial water with submolecular resolution by atomic force microscopy. *Nat. Commun.* **9**, 122 (2018).
35. Shiotari, A. & Sugimoto, Y. Ultrahigh-resolution imaging of water networks by atomic force microscopy. *Nat. Commun.* **8**, 14313 (2017).
36. Meier, M. et al. Water agglomerates on Fe_3O_4(001). *Proc. Natl Acad. Sci. USA* **115**, E5642–E5650 (2018).
37. Ma, R. et al. Atomic imaging of the edge structure and growth of a two-dimensional hexagonal ice. *Nature* **577**, 60–63 (2020).
38. Malkin, T. L., Murray, B. J., Brukhno, A. V., Anwar, J. & Salzmann, C. G. Structure of ice crystallized from supercooled water. *Proc. Natl Acad. Sci. USA* **109**, 1041–1045 (2012).
39. Pan, D. et al. Surface energy and surface proton order of ice Ih. *Phys. Rev. Lett.* **101**, 155703 (2008).
40. Binnig, G., Rohrer, H., Gerber, C. & Weibel, E. 7 × 7 reconstruction on Si(111) resolved in real space. *Phys. Rev. Lett.* **50**, 120–123 (1983).

Publisher's note Springer Nature remains neutral with regard to jurisdictional claims in published maps and institutional affiliations.

Springer Nature or its licensor (e.g. a society or other partner) holds exclusive rights to this article under a publishing agreement with the author(s) or other rightsholder(s); author self-archiving of the accepted manuscript version of this article is solely governed by the terms of such publishing agreement and applicable law.

© The Author(s), under exclusive licence to Springer Nature Limited 2024

Methods

Sample preparation

The Au(111) and Pt(111) single crystals were purchased from MaTeck. The Au(111) crystal was cleaned by repeated Ar^+ ion sputtering at around 1 keV and annealing at about 700 K for multiple cycles. The Pt(111) crystal was cleaned by Ar^+ ion sputtering at around 1 keV and annealing to 1,300–1,400 K, followed by heating at 1,000 K under the oxygen pressure of 1×10^{-7} mbar for 10–20 min to remove carbon impurities. The residual oxygen at the surface was removed by a final flash annealing at 1,300–1,400 K. Ultrapure water (Sigma Aldrich, 99.9%) was used and further purified under vacuum by three to five freeze-and-pump cycles to remove remaining gas impurities. Water molecules were dosed at low temperatures under the vacuum through a dosing tube, which is separated from clean Au(111)/Pt(111) substrates by 15 cm. We used a DT670 silicon diode (Lakeshore) for temperature sensing. To ensure the precision of temperature measurement, we installed diodes close to sample stages with good thermal contact. Using our custom-developed temperature control system, we achieved a standard deviation at the set-point temperature within 30 mK (Supplementary Fig. 1). To obtain a thick enough ice-Ih film independent of underlying metal surfaces, we first dosed water molecules at 135 K with a high deposition rate of 25 bilayers per minute for a duration of 25 min (Supplementary Fig. 1), followed by a slow growth process at different temperatures (105–160 K) with a deposition rate of 10 bilayers per hour for 2 h (Supplementary Fig. 1). All as-grown samples were quickly transferred to AFM scanner kept at 4.2 K for further AFM measurements (Supplementary Fig. 1), by using a wobble stick precooled by a 77-K stage on the outershield for over 1 hour. Considering the extremely slow dynamics of supercooled water molecules at the low temperatures (below 150 K), the ice surface structure during the cooling process in our experiment is essentially quasi-static[41].

STM and AFM measurements

All the experiments were performed at 5 K with combined non-contact AFM and STM systems from CASAcme (China) and Createc (Germany), by using a home-made qPlus sensor equipped with a tungsten tip (spring constant, $k_0 \approx 1{,}800$ N m^{-1}; resonance frequency, $f_0 = 30.4$ kHz; quality factor, $Q \approx 100{,}000$). All AFM data were measured at 5 K under ultrahigh vacuum ($<3 \times 10^{-10}$ mbar). All the AFM topographic (z) images and the AFM frequency-shift (Δf) images were obtained with the CO-functionalized tips in constant-frequency-shift or constant-height modes, respectively. The details of the substrates for the ice growth are summarized in Supplementary Table 2. The oscillation amplitude of AFM imaging is 200 pm if not specifically mentioned. The tip height in AFM imaging refers to the largest tip height (set as 0 pm) during the height-dependent imaging process, where the contrasts of H-up water molecules can be fairly discerned. Only the relative heights between images have a certain reference value. Image processing was performed by Nanotec WSxM[42].

Functionalizing the tip apex with a CO molecule is crucial to achieve atomic resolution. As the well-established process for preparing a CO-terminated tip is typically carried out in STM mode on conductive substrates, it has been challenging to use the CO tip to scan completely insulating substrates such as bulk ices. In this work, we developed a general procedure to prepare the CO tip for any insulating substrates:

1. The CO tip was first obtained by positioning the tip over a CO molecule on the Au(111) surface at a set point of 100 mV and 10 pA in STM mode, followed by increasing the current to 400 pA. The quality of the obtained CO tip was checked by the STM image of a CO molecule and the frequency-shift versus distance curve taken above the Au(111) surface. To ensure tip stability, a preliminary tip approach was performed on the Au sample.
2. The Au sample was quickly replaced with the precooled ice sample (5 K) and the CO tip was kept at low temperature (5 K). To prevent CO desorption from the tip apex during the sample exchange, we considerably enhanced the cooling efficiency by optimizing the thermal contact between the cooling stage and the scanner.
3. To avoid changing the CO tip during the approach process, the tip was approached to the ice surface in AFM mode at an extremely low speed with a large oscillation amplitude (set point, −100 mHz; oscillation amplitude, 1 nm; approaching time for each step, 6 s; waiting time after each step, 1.5 s).
4. After the tip approach, we started the AFM imaging at the tip height of 2 nm (referenced to the set point, −100 mHz) to locate flat areas and to keep the CO tip intact. Through the above steps, the probability of successful tip preparation reaches up to 90%.

DFT calculations

DFT calculations were performed using the Vienna Ab initio Simulation Package (VASP version 6.2)[43,44]. Projector-augmented wave pseudopotentials were used with a cut-off energy of 550 eV for the expansion of the electronic wavefunctions[45]. Van der Waals corrections for dispersion forces were considered using the 'optB86b-vdW' functional[46,47]. In all DFT calculations, the ice-Ih substrate was modelled as a four-bilayer slab structure, which was first relaxed as in the bulk with periodic conditions in all three directions. Then the newly grown bilayer was added to the substrate and the bottom three bilayers were fixed for subsequent calculations. In the topmost bilayer of the simulated PLS structures, the water molecules directly surrounding the PLS were allowed to relax. The water molecules positioned farther away from the PLS were arranged to replicate the experimental condition, with their positions fixed. The simulation box for the $\sqrt{19} \times \sqrt{19}$ superstructure was a prism with a height of 40 Å, and a rhombic cross-section with sides of 18.89 Å and angles of 60°, which corresponds to the two-dimensional unit cell of the superstructure. The simulation box for the $2\sqrt{19} \times \sqrt{19}$ superstructure was created by replicating the former simulation box, doubling its size. For the ideal 1×1 surface, which serves as a reference for energy comparison, the simulation box dimensions are identical to those used for the superstructures. The size of simulation box used for PLS calculations is 17.68 Å × 45.94 Å × 34.45 Å. For all these calculations, only the Γ point was used and the thickness of the vacuum slab in z direction was larger than 15 Å. The geometry optimizations were carried out at fixed volume with a force criterion of 0.02 eV Å^{-1}.

Simulations of AFM images

The Δf images were simulated with a molecular mechanics model, based on the methods described previously[48,49]. We used the following parameters for the flexible probe–particle tip model: effective lateral stiffness $k = 0.75$ N m^{-1} and effective atomic radius $R_c = 1.661$ Å. A quadrupole-like charge distribution at the tip apex was used to simulate the CO tip with $q = -0.10e$ (e is the elementary charge and q is the magnitude of quadrupole charge at the tip apex). The electrostatic potentials used in AFM simulations were obtained from DFT calculations. The parameters r (van der Waals radius) and ε (potential well depth) of the Lennard–Jones pairwise potentials for the O and H atoms used in AFM simulations are: $r_H = 1.487$ Å, $\varepsilon_H = 0.681$ meV, $r_O = 1.661$ Å and $\varepsilon_O = 9.106$ meV. The tip height in the AFM simulations is defined as the vertical distance between the metal tip apex and the topmost layer of the substrate. The oscillation amplitudes of the simulated AFM images are 200 pm.

Molecular-dynamics simulations

We performed deposition simulations of water molecules on the ice-Ih surface at 180 K using large-scale molecular-dynamics simulations. We used a monoatomic model (mW) for water–water interactions[50], which consists of short-ranged two-body and three-body non-bonding potentials without explicitly including H atoms. The velocity Verlet algorithm was used to integrate the equations of the motion with a time

step of 10 fs. The pressure was controlled by a Nose–Hoover barostat with a relaxation time of 5 ps, and the temperature was controlled by Langevin thermostat with a relaxation time of 0.5 ps. Periodic boundary conditions were applied in all three directions of the simulation box. All molecular-dynamics simulations were carried out using the Large-scale Atomic/Molecular Massively Parallel Simulator (LAMMPS) package[51].

The deposition process was initiated on an 8-bilayer ice-Ih slab with dimensions of 352.2 Å × 366.1 Å. The ice slab contained 15,360 water molecules per bilayer, and its density was adjusted to match the results obtained from an independent constant-pressure and constant-temperature (NPT) ensemble simulation under the specified temperature and vacuum conditions. The simulations were performed in a constant-volume and constant-temperature (NVT) ensemble, with the bottom four bilayers kept rigid. The water molecules, located at approximately 25 Å above the ice-Ih surface, were given initial velocities of 5 Å ps^{-1} in the direction towards the ice-Ih surface.

First, we introduced a total number of 15,360 water molecules (the same number as in 1 bilayer) to the simulation, deposited at a rate of 1 molecule every 10 ps. Following that, the system was relaxed for 100 ns for equilibration. Nevertheless, mixed Ih- and Ic-stacking nanodomains, as well as defective boundaries with 5–7–8 rings, remained on the surface, while the lower bilayers retained the Ih-stacking pattern. Then, 15,360 additional water molecules were introduced to the surface, with the same deposition rate as used before. Finally, the structure was allowed to undergo free evolution for 2,500 ns without further adding water molecules. During this procedure, the Ic-stacking nanodomains that existed in the previously deposited bilayer (now the second topmost bilayer) underwent a gradual transformation into Ih stacking (Extended Data Fig. 2 and Supplementary Video 1). This demonstrates that the intra-bilayer stacking disorder occurs at only the topmost surface.

To assess the stability of the surface superstructure at 120 K, we employed three different models: a monoatomic model (mW)[50], a full atomic model (TIP4P/Ice)[52] and the CCSD (T) precision model (MB-pol)[53–55]. Initially, we adjusted the density of each structure to match the results obtained from an independent NPT ensemble simulation at 120 K and vacuum conditions for each model. Subsequently, simulations were conducted in an NVT ensemble at 120 K, incorporating a vacuum gap in the structural set-up. Owing to substantial differences in computational resource requirements among various models, we conducted simulations with varied durations, utilizing models of different sizes as large as possible within our computational capacity. For the mW model, simulations were performed in a box with dimensions of 198.8 Å × 191.08 Å, lasting 1,000 ns. For the TIP4P/Ice model, simulations were performed in a box measuring 101.56 Å × 97.63 Å, lasting 10 ns. Finally, for the MB-pol model, simulations were performed in a box with dimensions of 33.85 Å × 39.05 Å, lasting 1 ns. The results indicated that the superstructure maintains stability in all models, without any water molecules departing from their lattice positions or any changes in the H-bonding topology.

DFT-calculated formation energies of ice surfaces with different S_{OH}

To distinguish different distributions of the dangling OH bonds at the surface, we define an order parameter similar to previous studies[39]:

$$S_{OH} = \sum_{\substack{i,j \\ i<j}}^{N_{OH}} \theta(r_{ij}),\ \text{in which } \theta(r_{ij}) = \begin{cases} 1, r_{ij} < 5.5\ \text{Å} \\ 0, r_{ij} < 5.5\ \text{Å} \end{cases} \quad (1)$$

where N_{OH} is the number of dangling OH bonds in the upper part of the topmost bilayer. S_{OH} describes the total number of nearest-neighbour dangling OH pairs within an area equivalent to the unit cell in $\sqrt{19} \times \sqrt{19}$ phase. The truncation distance is 5.5 Å, including only all nearest-neighbour undercoordinated water pairs connected by the same lower-lying water molecule in superstructures (Extended Data Fig. 10). To be consistent with the observed experimental value in superstructures (1:1.14), the ratio of H-up to O-up water molecules in the upper part of the topmost ice bilayer is chosen as 7:8. Accordingly, the ratio of H-up to O-up water molecules in the upper part of the second topmost bilayer within the Ih substrate is 9:10. The formation energy per water molecule in the topmost bilayer is defined as

$$E_{form} = \frac{E_{total} - E_{substrate} - N_{growth} \times E_{H_2O}}{N_{growth}} \quad (2)$$

where N_{growth} is the total number of water molecules in the topmost bilayer, E_{total} represents the total energy of the newly grown system including the ice-Ih substrate and the newly deposited bilayer, $E_{substrate}$ represents the total energy of the ice-Ih substrate containing four bilayers, and E_{H_2O} is the energy of isolated water molecule in vacuum. To accurately compare the relative stability of the ideal surface and the two superstructures (with the same $E_{substrate}$), all ice surfaces with different S_{OH} in Fig. 3 are based on an identical Ih substrate, with the ratio in accordance with experiments (H_{up}:O_{up} = 9:10) and an intermediate order parameter of H-up water molecules (S_{OH} = 11). The lowest value of the order parameter S_{OH} calculated in the superstructures is 2, whereas for the ideal 1 × 1 surface, it is 8.

From the calculated isosurface of total charge (Supplementary Fig. 7), we can see that the negative charge distribution at the surface is uniform. The positively charged H atom, which 'dangles' out of the surface, has an important role in surface electrostatic repulsive energy. By utilizing a classical electrostatics model, we can gain insight into the strong dependence of the formation energy on the proton arrangement at the surface, showing linear correlation for all the three surfaces. Specifically, we can write E_{form} as

$$E_{form} = E_{form}^{S_{OH}=0} + \Delta E_{HH} = E_{form}^{S_{OH}=0} + \frac{q_{dangling}^{\ 2}}{\overline{r_{HH}}} \times S_{OH} = E_{form}^{S_{OH}=0} + k \times S_{OH} \quad (3)$$

where $E_{form}^{S_{OH}=0}$ is the formation energy without considering any electrostatic repulsion between OH bonds (S_{OH} = 0), E_{HH} is the excess energy due to the additional electrostatic repulsion between nearest-neighbour dangling OH pairs, $q_{dangling}$ is the equivalent charge quantity of a H atom, and $\overline{r_{HH}}$ is the average distance between nearest-neighbour dangling OH bonds. The slope k is expected to be directly proportional to $q_{dangling}^{\ 2}$ for dangling OH pairs, and is inversely proportional to $\overline{r_{HH}}$. Bader calculations reveal that the values of $q_{dangling}$ for the two superstructures and the ideal surface are identical ($q_{dangling}$ = 0.39e). The reduced slope observed in the superstructures, compared with the ideal surface, can be attributed to the larger $\overline{r_{HH}}$. This is probably due to the presence of fewer undercoordinated water molecules in the superstructures.

DFT-calculated surface energies of ice surfaces with different S_{OH}

Similar to formation energy per water molecule, we can also define surface energy per unit area as

$$E_{surface} = \frac{E_{total} - (N_{substrate} + N_{growth}) \times E_{H_2O}^{bulk}}{S} \quad (4)$$

where $N_{substrate}$ is the number of molecules in the ice-Ih substrate, N_{growth} is the total number of molecules in the topmost newly deposited bilayer, E_{total} represents the total energy of the newly grown system including the ice-Ih substrate and the newly deposited bilayer, and $E_{H_2O}^{bulk}$ represents the energy of each molecule as in ice-Ih bulk. $E_{surface}$ represents the combined surface energies of the reconstructed (or unreconstructed) topmost bilayer and the frozen bottom bilayer. When comparing the surface energies of different structures, the surface energies of the frozen bottom bilayers cancel each other out[56].

Consistent with E_{form}, a smaller value for $E_{surface}$ indicates a higher stability of the surface.

We used the same order parameter S_{OH} as defined in the 'DFT-calculated formation energies of ice surfaces with different S_{OH}' section and calculated the surface energy per unit area of all ice surfaces with different S_{OH} (Extended Data Fig. 7). All trends align consistently with those in Fig. 3. This underscores that despite the switch to surface energy, the conclusion that the superstructures with homogeneous arrangements of dangling OH bonds ($S_{OH} \leq 5$) tend to be more stable than the ideal 1 × 1 surface remain unchanged.

Comparison of AFM results with those from other experimental methods

To gain deeper insights into the field of ice surfaces, we compared our real-space AFM results of ice surfaces with previous spectroscopic data. To facilitate a clear comparison, we organized our discussion based on the different techniques involved. Overall, spectroscopic evidence generally supports the existence of reconstruction on ice surfaces and suggests the local ordering of dangling OH bonds. However, the exact nature of reconstruction is not clear.

Low-energy electron diffraction experiments have revealed a six-fold symmetric pattern in previous studies[18,57]. However, considering that the probe depth is at least 10 Å, these results mainly reflect the 1 × 1 unreconstructed phase at the subsurface and the Ih and Ic domains at the surface. The surface superstructure is not visible in the low-energy electron diffraction results, probably owing to its very narrow temperature range.

Crystalline ice layers in the bulk were also evidenced by X-ray absorption spectroscopy[23], with 50 nm probing depth. By varying probing depths, spectral differences between surface and bulk were observed, indicating a distortion in the hexagonal lattice within the first few bilayers at the surface. These results could be associated with the defective boundaries between the Ih and Ic domains on the surface, which were identified in our study.

Previous helium-atom scattering experiments revealed inconsistent results: a 1 × 1 ideal surface[11] and a reconstructed surface characterized by broad and weak p (2.1 × 2.1) diffraction peaks[22]. To directly compare our AFM images with the diffraction results, we performed a two-dimensional FFT analysis of different ice surfaces, shown in Supplementary Fig. 6, and demonstrated that those subpeaks in helium-atom scattering could be attributed to short-range 2.1 × 2.1 order of dangling OH bonds along defective boundaries. Such a local order reflects the uniform distribution of dangling OH bonds at the next-nearest-neighbour sites. Different characteristic next-nearest distances at Ic/Ih boundaries and in disordered regions leads to the fluctuation of this distance. However, the stability of the superstructure is not directly related to this ordering, but dominated by the electrostatic repulsive energy between the nearest-neighbour dangling OH pairs, which can be described by the order parameter S_{OH} as shown in Fig. 3.

Molecular-level details of ice surfaces could be unveiled through a combination of sum frequency generation (SFG) and molecular-dynamics calculations. Molecular-dynamics calculations based on models with an equal number of H-up and O-up water molecules on the surface often show good agreement with SFG spectra[25,26,58]. By contrast, recent heterodyne-detected SFG studies revealed that ice Ih surfaces show H-up polarization at both 100 K and 13 K (refs. 27,59). However, our experimental observation shows very slight polarization at the surface of superstructure, with a ratio of H-up to O-up water molecules of 1:1.14.

Besides investigating the crystalline structure of ice surfaces, SFG is also a powerful method to study the premelting of ice surface. So far, most SFG experiments have been conducted at elevated temperatures (above 150 K)[12,24,26]. It has been demonstrated that the outermost ice layer is already disordered at 250 K (ref. 24). In addition, a decrease in the fraction of dangling OH bonds with increasing temperature was observed below 200 K (ref. 26). As the ice layers would desorb above 150 K under ultrahigh vacuum, our experiments were focused on the initial stage of the premelting process below 150 K.

Our experimental temperature range aligns with that of the paper[25] where the disordering onset was noted at 120 K, consistent with our findings. In addition, they observed a decrease in the number of dangling OH bonds above 120 K. To facilitate direct comparison, we conducted a statistical analysis on the ratio of O-up to H-up water molecules at varying growth temperatures in our experiments, yielding a similar trend (Supplementary Fig. 12).

To allow a more direct comparison, we summarized the above discussions as Supplementary Table 1.

Data availability

The tabulated data used to create the figures and the Extended Data figures, as well as the molecular-dynamics trajectories, have been deposited at *Zenodo* (https://doi.org/10.5281/zenodo.10827371)[60]. All other data needed to evaluate the conclusions in the paper are present in the paper or Supplementary Information.

41. Cerveny, S., Mallamace, F., Swenson, J., Vogel, M. & Xu, L. Confined water as model of supercooled water. *Chem. Rev.* **116**, 7608–7625 (2016).
42. Horcas, I. et al. WSXM: a software for scanning probe microscopy and a tool for nanotechnology. *Rev. Sci. Instrum.* **78**, 013705 (2007).
43. Kresse, G. & Hafner, J. Ab initiomolecular dynamics for liquid metals. *Phys. Rev. B* **47**, 558–561 (1993).
44. Kresse, G. & Furthmuller, J. Efficient iterative schemes for ab initio total-energy calculations using a plane-wave basis set. *Phys. Rev. B* **54**, 11169–11186 (1996).
45. Kresse, G. & Joubert, D. From ultrasoft pseudopotentials to the projector augmented-wave method. *Phys. Rev. B* **59**, 1758–1775 (1999).
46. Klimeš, J., Bowler, D. R. & Michaelides, A. Chemical accuracy for the van der Waals density functional. *J. Phys. Condens. Matter* **22**, 022201 (2010).
47. Klimeš, J., Bowler, D. R. & Michaelides, A. Van der Waals density functionals applied to solids. *Phys. Rev. B* **83**, 195131 (2011).
48. Hapala, P. et al. Mechanism of high-resolution STM/AFM imaging with functionalized tips. *Phys. Rev. B* **90**, 085421 (2014).
49. Hapala, P., Temirov, R., Tautz, F. S. & Jelínek, P. Origin of high-resolution IETS-STM images of organic molecules with functionalized tips. *Phys. Rev. Lett.* **113**, 226101 (2014).
50. Molinero, V. & Moore, E. B. Water modeled as an intermediate element between carbon and silicon. *J. Phys. Chem. B* **113**, 4008–4016 (2009).
51. Plimpton, S. Fast parallel algorithms for short-range molecular-dynamics. *J. Comput. Phys.* **117**, 1–19 (1995).
52. Abascal, J. L. F., Sanz, E., García Fernández, R. & Vega, C. A potential model for the study of ices and amorphous water: TIP4P/Ice. *J. Chem. Phys.* **122**, 234511 (2005).
53. Reddy, S. K. et al. On the accuracy of the MB-pol many-body potential for water: interaction energies, vibrational frequencies, and classical thermodynamic and dynamical properties from clusters to liquid water and ice. *J. Chem. Phys.* **145**, 194504 (2016).
54. Cisneros, G. A. et al. Modeling molecular interactions in water: from pairwise to many-body potential energy functions. *Chem. Rev.* **116**, 7501–7528 (2016).
55. Bore, S. L. & Paesani, F. Realistic phase diagram of water from "first principles" data-driven quantum simulations. *Nat. Commun.* **14**, 3349 (2023).
56. Torres, E. & DiLabio, G. A. A density functional theory study of the reconstruction of gold (111) surfaces. *J. Phys. Chem. C* **118**, 15624–15629 (2014).
57. Materer, N. et al. Molecular surface structure of ice(0001): Dynamical low-energy electron diffraction, total-energy calculations and molecular dynamics simulations. *Surf. Sci.***381**, 190–210 (1997).
58. Smit, W. J. et al. Observation and identification of a new OH stretch vibrational band at the surface of ice. *J. Phys. Chem. Lett.* **8**, 3656–3660 (2017).
59. Nojima, Y., Shioya, Y., Torii, H. & Yamaguchi, S. Hydrogen order at the surface of ice Ih revealed by vibrational spectroscopy. *Chem. Commun.* **56**, 4563–4566 (2020).
60. Hong, J. et al. Imaging surface structure and premelting of ice Ih with atomic resolution. *Zenodo* https://doi.org/10.5281/zenodo.10827370 (2024).
61. Nguyen, A. H. & Molinero, V. Identification of clathrate hydrates, hexagonal ice, cubic ice, and liquid water in simulations: the CHILL+ algorithm. *J. Phys. Chem. B* **119**, 9369–9376 (2014).

Acknowledgements We thank C. Wang and X. Zeng for discussions and the computational resources provided by the TianHe-1A, TianHe II supercomputer, High-performance Computing Platform of Peking University. This work was supported by the National Key R&D Program under grant 2021YFA1400500; the National Natural Science Foundation of China under grants 11888101, 92361302, 11935002, 12250001, U22A20260 and 12204039; the Strategic Priority Research Program of Chinese Academy of Sciences under grant XDB28000000; the Key R&D Program of Guangdong Province under grant 2020B010189001; the China Postdoctoral Science Foundation under grants BX20230021 and 2023T160011. D.P. acknowledges support from the Hong Kong Research Grants Council (GRF-16306621) and National Natural Science

Foundation of China through the Excellent Young Scientists Fund 22022310. Y.J. acknowledges support from the New Cornerstone Science Foundation through the New Cornerstone Investigator Program and the XPLORER PRIZE.

Author contributions Y.J. and E.-G.W. designed and supervised the project. J.H. and Y.T. performed the AFM measurements with X.L. and D.G. T.L., Y.S., B.T. and L.-M.X. performed ab initio DFT calculations, molecular-dynamics simulations and AFM simulations. Y.J., E.-G.W., L.-M.X., D.P., J.C., J.G., J.H., Y.T., T.L., X.L., Y.S., D.G., Z.Y., J.-D.G., B.T. and D.C. analysed the data. Y.J., J.H., Y.T., T.L., L.-M.X. and E.-G.W. wrote the paper with input from all other authors. The paper reflects the contributions of all authors.

Competing interests The authors declare no competing interests.

Additional information

Supplementary information The online version contains supplementary material available at https://doi.org/10.1038/s41586-024-07427-8.

Correspondence and requests for materials should be addressed to Ye Tian, Li-Mei Xu, En-Ge Wang or Ying Jiang.

Peer review information *Nature* thanks Yoshiaki Sugimoto and the other, anonymous, reviewer(s) for their contribution to the peer review of this work.

Reprints and permissions information is available at http://www.nature.com/reprints.

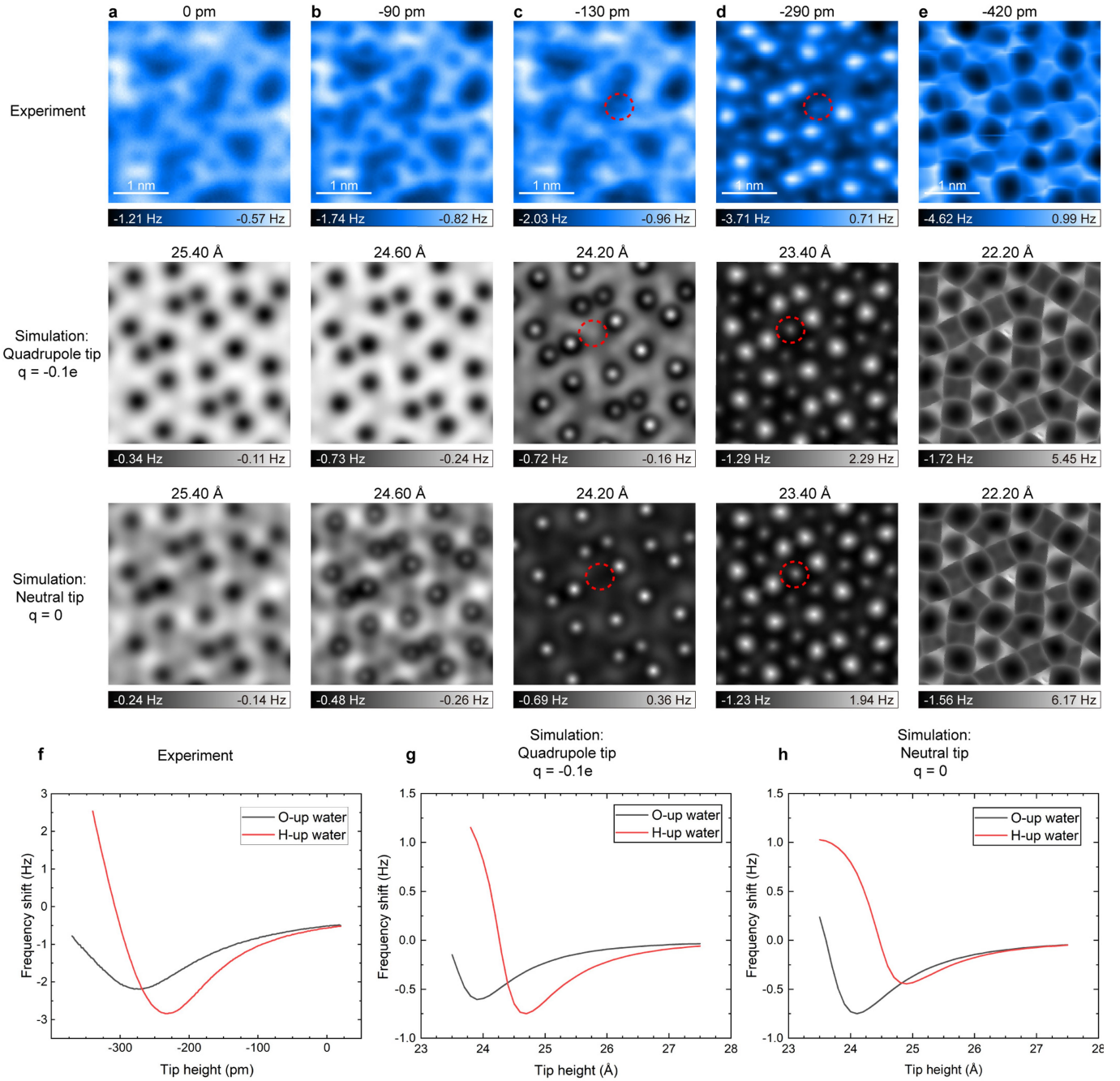

Extended Data Fig. 1 | Height-dependent experimental and simulated Δf images with quadrupole/neutral tips. a-e, Experimental (upper) and simulated Δf images with quadrupole (d_z^2, $q = -0.1$ e, middle) and neutral ($q = 0$ e, lower) tips. Simulated images acquired by the quadrupole tip agree better with the experimental results. At a larger tip height, the H-up water molecules are visualized as individual depressions both by quadrupole and neutral tips (middle and lower panels in **a**), due to long-range vdW attraction from the higher O atoms (~13 pm). However, the electrostatic force between the quadrupole tip and H atoms can enlarge the attractive interaction, leading to much larger force contrast. When the tip height is further decreased, the H-up water molecules evolve into bright protrusions due to the Pauli repulsion. Meanwhile, because of the electrostatic repulsion, O-up water molecules also show bright feature with the quadrupole tip, indicated by red dashed circles in upper and middle panels in **c**. In contrast, the O-up water molecules are revealed as dark features by the neutral tip, indicated by the red dashed circle in the lower panel in **c**. Tip heights are given above each image. **f-h**, Experimental (**f**, oscillation amplitude, 40 pm) and simulated (**g**,**h**, oscillation amplitude, 200 pm) frequency-shift (Δf) versus distance curves above an H-up water molecule (red line) and an O-up water molecule (black line). The experimental (**f**) and simulated (**g**, the quadrupole tip) curves show qualitatively similar behavior, where the turning point of the H-up water molecule occurs at a larger tip height and its minimum Δf is deeper than that of the O-up water molecule. The curve acquired by the neutral tip (**h**) shows the opposite behavior, where the minimum Δf of the O-up water molecule is deeper. Such a difference arises from the attractive (repulsive) force between the positively (negatively) charged H (O) and the negatively charged CO tip.

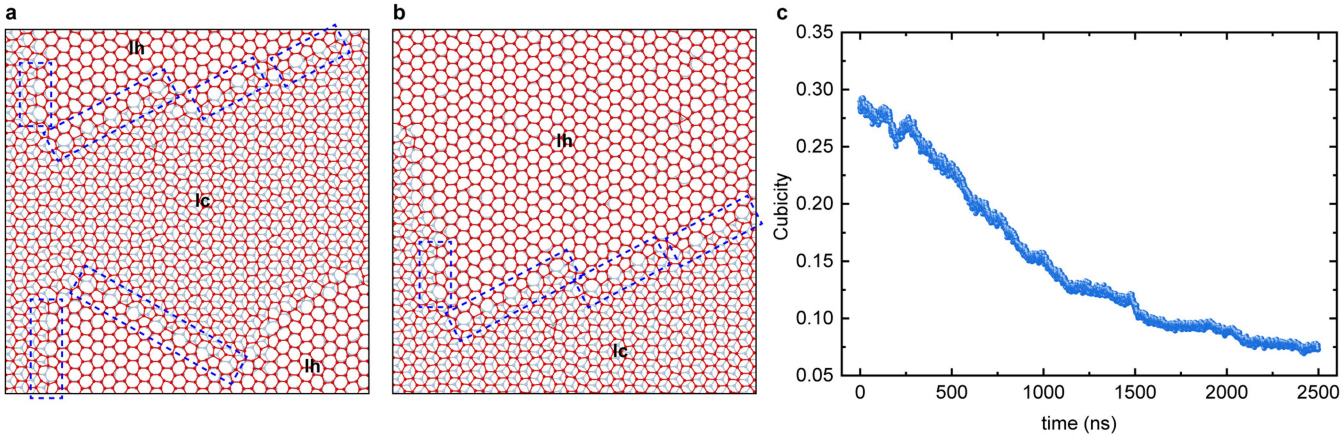

Extended Data Fig. 2 | Intra-bilayer stacking disorder existing only on the surface. a, **b**, The snapshots of MD simulations of intra-bilayer stacking disorder on the topmost surface. The hexagonal surface bilayer was grown on an Ih substrate after an equilibration period of 2500 ns. To see more clearly, we extracted two 12 nm × 12 nm images from the original calculated image. Typical "55-8-55" line defects between the Ic and Ih domains at the surface are denoted by blue dashed lines. It should be mentioned that the mW potential does not explicitly include the individual H atoms. O atoms in the topmost bilayer and the bulk are denoted as red and light blue spheres, respectively. **c**, The evolution of the second topmost bilayer after the deposition of a new surface bilayer. Water molecules with cubic and hexagonal ice order are identified using CHILL +[61] and the cubicity is defined as the ratio of the number of Ic-stacking water molecules to the total number of molecules in both Ic and Ih-stacking patterns within the second topmost bilayer. Upon deposition of a new bilayer and subsequent equilibration at 180 K, there is a gradual decrease in the area of Ic-stacking nanodomains that existed in the previously deposited bilayer (now the second topmost bilayer) with time (Supplementary Video 1). Consequently, this clearly indicates that the intra-bilayer stacking disorder only exists on the surface.

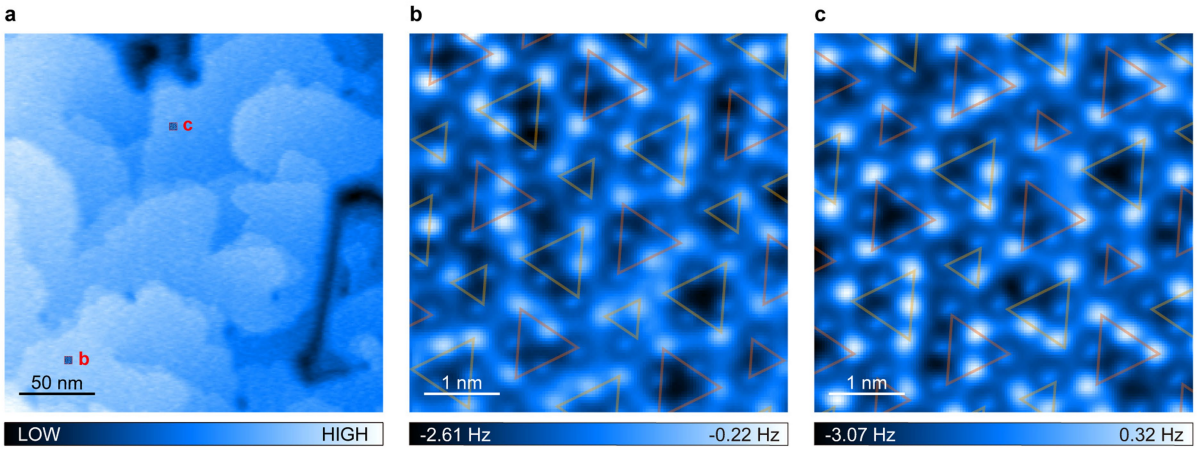

Extended Data Fig. 3 | The long-range order of superstructures. a, The constant-frequency-shift AFM image of the overall ice surface, acquired at the set point of −100 mHz. Two zoom-in areas within different terraces are spaced 170 nm apart, indicated by letters b and c. **b**, **c**, Constant-height AFM images corresponding to the insets in a, depicting perfect superstructures with the same orientation. Superstructures exhibit long-range order and could extend across entire terraces. The orange and yellow triangles represent tetrahedron structures in different stacking types.

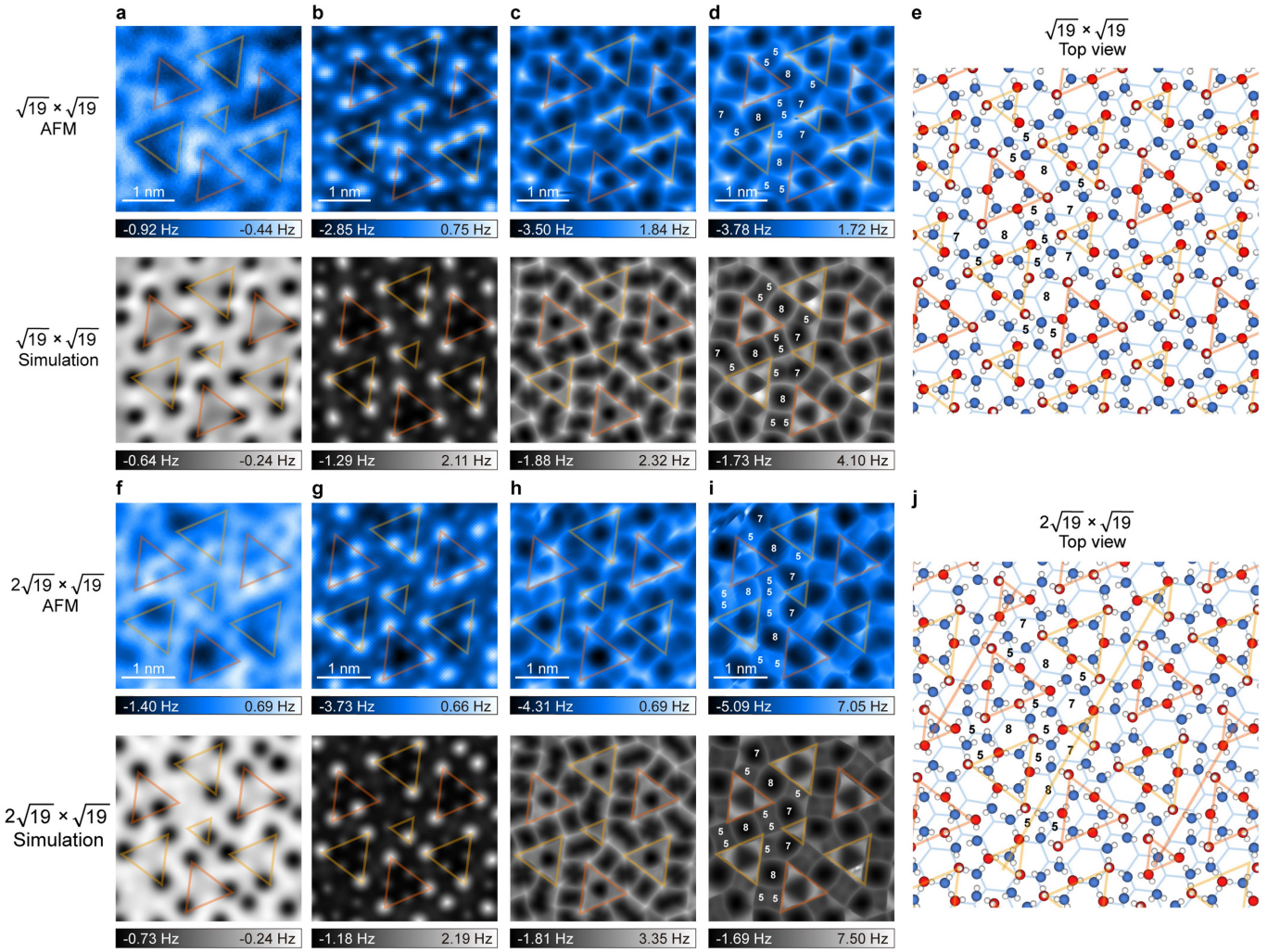

Extended Data Fig. 4 | Detailed AFM characterization of the $\sqrt{19} \times \sqrt{19}$ and $2\sqrt{19} \times \sqrt{19}$ superstructures. a-d, Zoom-in constant-height AFM images and the simulations of the pinwheel-like structure in the $\sqrt{19} \times \sqrt{19}$ phase at tip heights of 0 pm/24.60 Å, −190 pm/23.50 Å, −240 pm/22.60 Å and −270 pm/22.30 Å, respectively. **e**, Top view of the schematic $\sqrt{19} \times \sqrt{19}$ phase. All single-tetrahedron structures have the same stacking type, showing only the "55-8-57" boundary. **f-i**, Zoom-in constant-height AFM images and the simulations of the pinwheel-like structure in the $2\sqrt{19} \times \sqrt{19}$ phase at tip heights of 0 pm/24.60 Å, −240 pm/23.50 Å, −290 pm/22.50 Å and −330 pm/22.10 Å, respectively. **j**, Top view of the schematic $2\sqrt{19} \times \sqrt{19}$ phase. The single-tetrahedron structures with the same stacking type are in a stripe pattern, showing three types of boundaries ("57-8-57", "55-8-55", and "55-8-57"). The orange and yellow triangles represent tetrahedron structures with different stacking types. H and O atoms of the upper-lying and lower-lying water molecules in the topmost bilayer are denoted as white, red and dark blue spheres, respectively. Bilayers below the surface are shown in light blue.

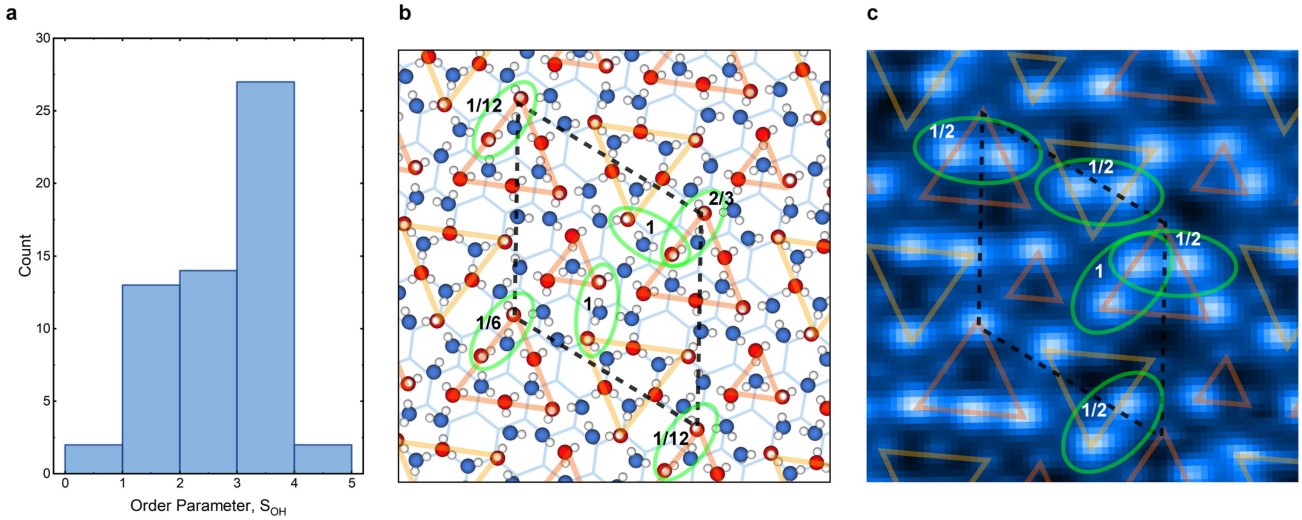

Extended Data Fig. 5 | Distribution of S_{OH} in experimental superstructures. **a**, The statistics of S_{OH} in two superstructures in experiments. Although the experimentally obtained superstructures don't exhibit complete proton ordering due to the presence of residual entropy, we can divide the surface area into units that are equivalent to the unit cell in $\sqrt{19} \times \sqrt{19}$ phase for statistical analysis. The small S_{OH}s for superstructures in experiments ($S_{OH} \leq 5$) represent the homogeneous distribution of dangling OH bonds at the surface, with a dominant value of ~3. **b**, **c**, Typical surface structures of $S_{OH} = 1/12 + 2/3 + 1 + 1/12 + 1 + 1/6 = 3$ (calculated $\sqrt{19} \times \sqrt{19}$ phase) and $S_{OH} = 1/2 + 1/2 + 1/2 + 1 + 1/2 = 3$ (experimental). The contribution value of 1 in S_{OH} is assigned to both of the two nearest-neighboring dangling OH bonds that are located within the unit cell. For dangling OH bonds located at the boundary or corner, the contribution to S_{OH} is determined based on the proportion of their portion belonging to the unit cell. Pairs of nearest-neighbor dangling OH bonds are denoted by green circles. The orange and yellow triangles represent tetrahedron structures in different stacking types. H and O atoms of the upper-lying and lower-lying water molecules in the topmost bilayer are denoted as white, red and dark blue spheres, respectively. Bilayers below the surface are shown in light blue.

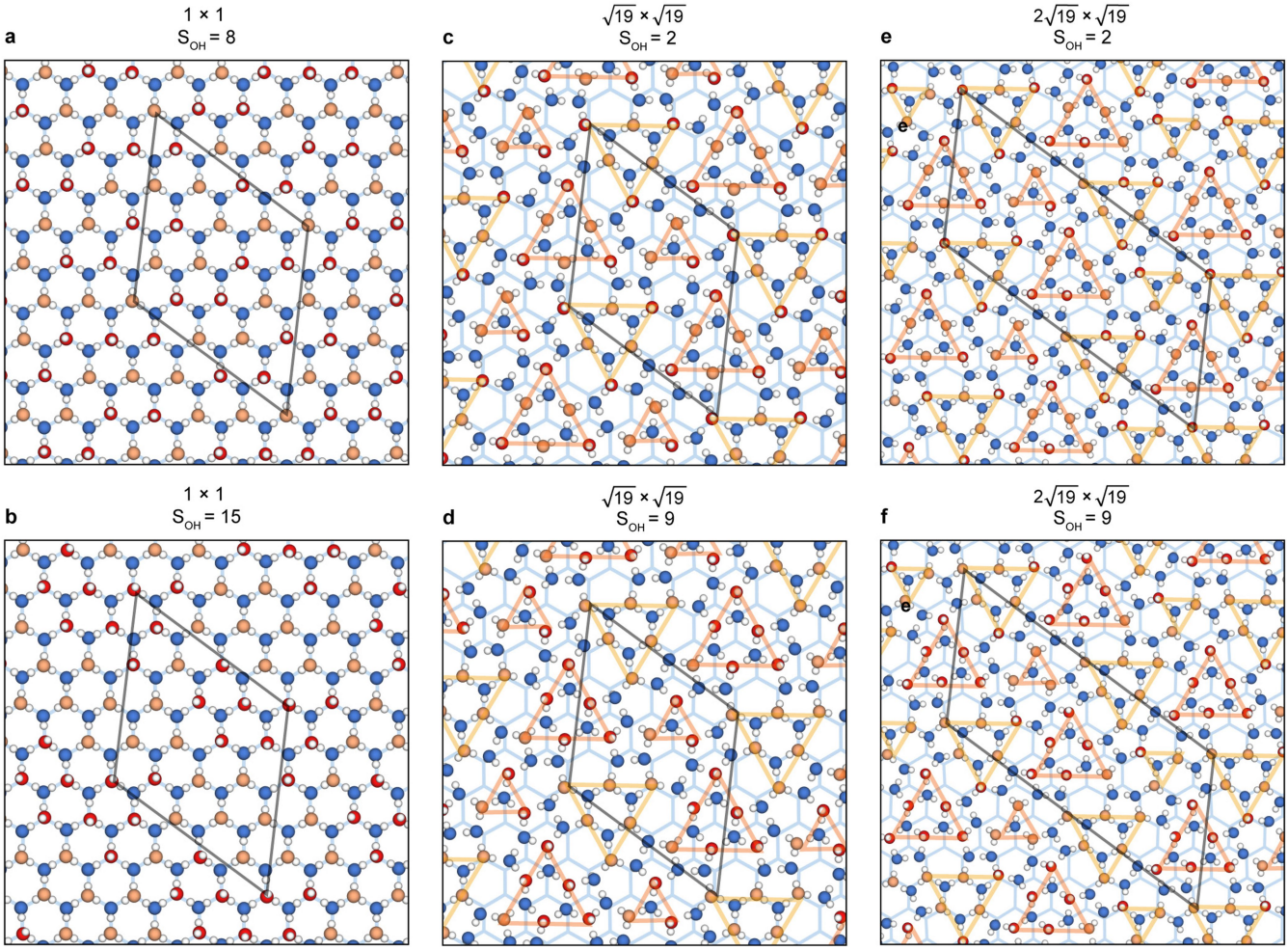

Extended Data Fig. 6 | Calculated ideal 1 × 1 surfaces and superstructures with different S_{OH}. **a**, **b**, Ideal 1 × 1 phase with S_{OH} = 8 and S_{OH} = 15, respectively. **c**, **d**, $\sqrt{19} \times \sqrt{19}$ phase with S_{OH} = 2 and S_{OH} = 9, respectively. **e**, **f**, $2\sqrt{19} \times \sqrt{19}$ phase with S_{OH} = 2 and S_{OH} = 9, respectively. The black lines indicate the areas used to determine the total number of nearest-neighbor dangling OH pairs. S_{OH} describes the total number of nearest-neighbor dangling OH pairs within an area equivalent to the unit cell of $\sqrt{19} \times \sqrt{19}$ phase. For $2\sqrt{19} \times \sqrt{19}$ phase, since its unit cell area is twice as large as that of $\sqrt{19} \times \sqrt{19}$ phase, the obtained S_{OH} should be divided by 2. The orange and yellow triangles represent tetrahedron structures in different stacking types. H and O atoms of the lower-lying water molecules in the topmost bilayer are denoted as white, and dark blue spheres, respectively. O atoms of H-up and O-up water molecules are denoted as red and yellow spheres, respectively. Bilayers below the surface are shown in light blue.

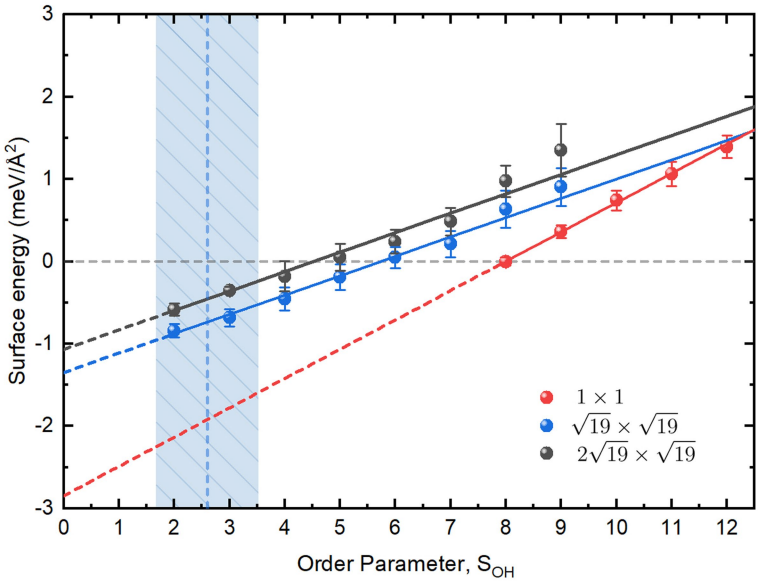

Extended Data Fig. 7 | Surface energies of different ice surface phases as a function of order parameter S_{OH}. Surface energy per unit area versus order parameter S_{OH} is derived by DFT-based energetic calculations. The zero energy is set to be the minimum surface energy of the ideal 1×1 surface, corresponding to $S_{OH} = 8$. All observed trends and curves are consistent with those presented in Fig. 3. A linear correlation between surface energy and S_{OH} is evident, and the superstructures with homogeneous arrangements of dangling OH bonds ($S_{OH} \leq 5$) tend to be more stable than the ideal 1×1 surface. For $\sqrt{19} \times \sqrt{19}$ and 1×1 phases, data points at each S_{OH} value represent the averaged formation energy calculated for eight surface structures with different H-bonding configurations and error bars represent their standard deviation. For the $2\sqrt{19} \times \sqrt{19}$ phase, only three surface structures at each S_{OH} were calculated. The dashed vertical line and shaded blue area represent the average $S_{OH} = 2.6$ and the standard deviation for superstructures obtained in experiment, respectively. The Ih substrate remains consistent in all phases, with a S_{OH} value of 11.

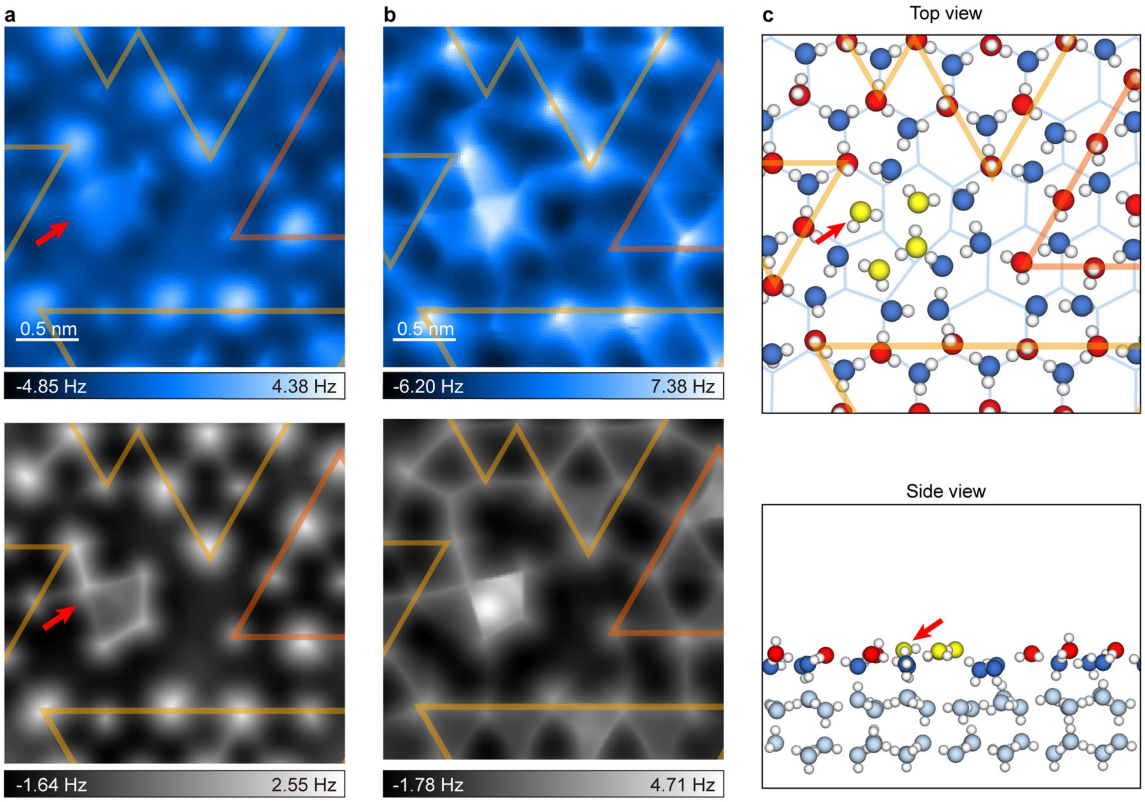

Extended Data Fig. 8 | The structure of PLS under a more disordered local environment than that in Fig. 4c–e. a,**b**, Constant-height experimental AFM images and simulations of the PLS at the intersection of multiple Ic and Ih domains. **c**, Top and side views of the PLS. The H-bonding network in the second topmost bilayer undergoes slight adjustments depending on the local environment of the surface PLS. Tip heights for **a**: −140 pm, 23.30 Å and **b**: −190 pm, 22.90 Å. The interstitial water molecule is indicated by the red arrow. O atoms of PLS are denoted as yellow spheres in the schematic models. H and O atoms of the upper-lying and lower-lying water molecules in the topmost bilayer are denoted as white, red and dark blue spheres, respectively. Bilayers below the surface are shown in light blue.

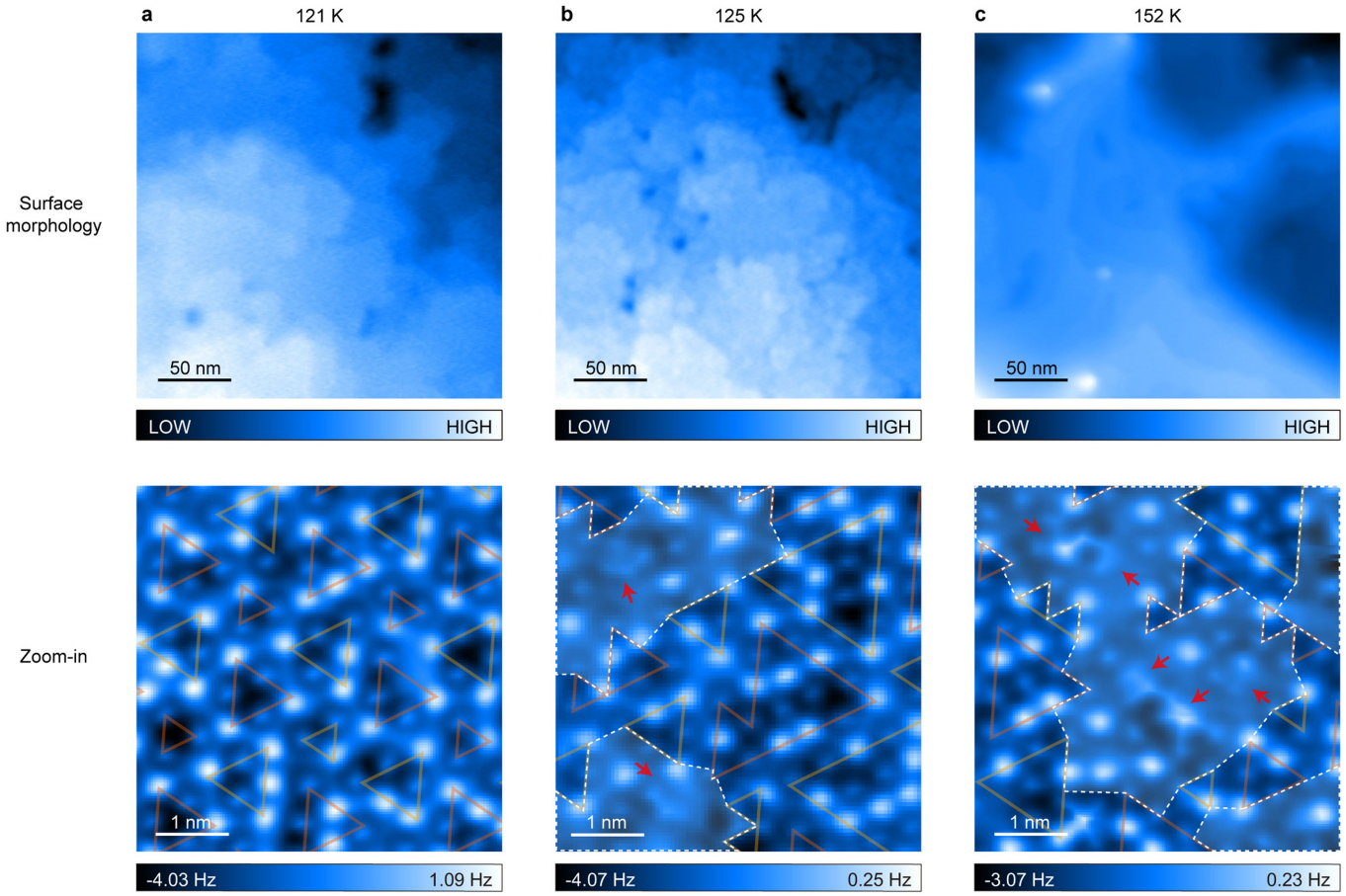

Extended Data Fig. 9 | Temperature-dependent surface morphology and high-resolution AFM images of ice surfaces. a-c, Constant-frequency-shift (upper) and corresponding constant-height (lower) AFM images of ice films grown at 121 K, 125 K and 152 K, respectively. As the temperature increases, the surface experiences a growing level of disorder due to the pre-melting process. The appearance of a deep valley in the surface morphology at 152 K arises from the desorption of water molecules in vacuum. The PLSs, the peripheries of Ic/Ih domains and the surface disorder area are indicated by red arrows, orange/yellow lines and white dashed lines, respectively. Constant-frequency-shift images were acquired at the set point of −100 mHz, −200 mHz and −100 mHz, respectively, all with 200-pm oscillation amplitude.

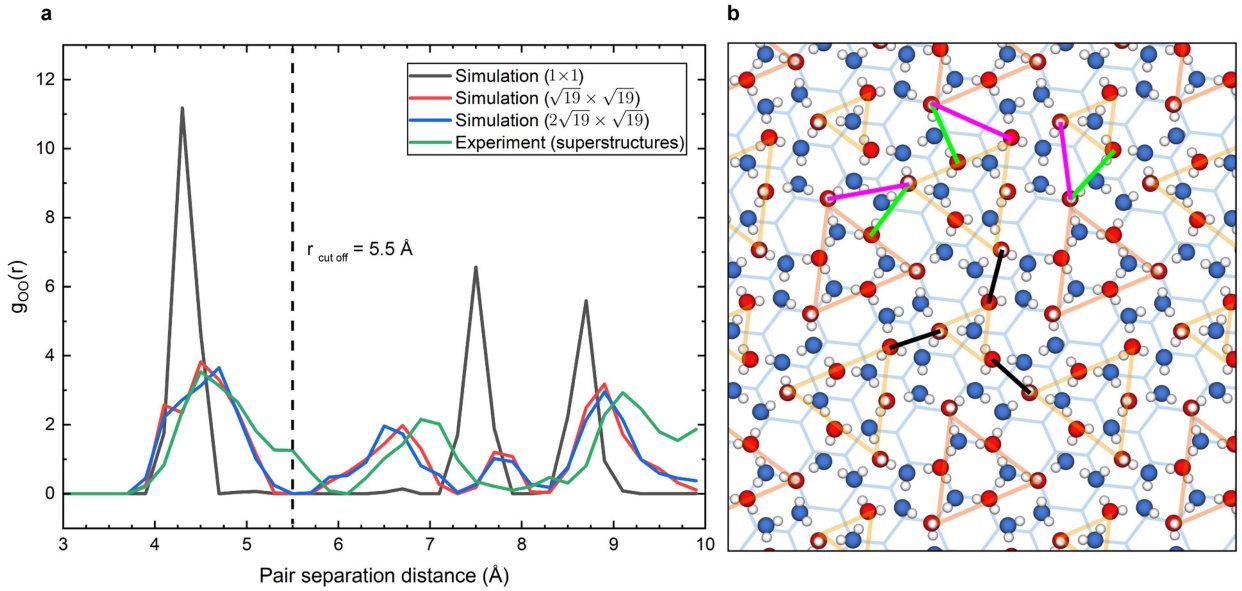

Extended Data Fig. 10 | The oxygen-oxygen radial distribution function (RDF) of two superstructures and the ideal 1 × 1 surfaces. a, The RDF graph containing both experimental and theoretical data. $g_{OO}(r)$ defines the probability of finding an O atom at a distance r from another O atom within the upper part of the topmost bilayer. The green curve is statistically derived from the AFM image of superstructures, with binomial smoothing. The black, red and blue curves are obtained by averaging all surface structures with different S_{OH} in simulation (64 structures for both ideal 1×1 phase and $\sqrt{19} \times \sqrt{19}$ phase, 29 structures for $2\sqrt{19} \times \sqrt{19}$ phase), using a bin size of 0.2 Å. The simulation results have good agreement with the experiment values. The calculated truncation distance of 5.5 Å effectively distinguishes the first nearest neighbors of the undercoordinated water molecules within the upper part of the topmost bilayer, consistent with the definition of S_{OH}. **b**, The top view of schematic $\sqrt{19} \times \sqrt{19}$ phase. In the superstructures, the nearest-neighbor peak (ranging from 3.8 to 5.4 Å) exhibits significant broadening compared to that of the ideal surface (ranging from 3.9 to 4.5 Å). Such a difference arises from the nearest-neighbor water molecules within the five, seven and eight-membered rings at the defective boundaries, indicated by black (average distance: 4.1 Å) and green (average distance: 4.9 Å) lines in **b**. Compared to the ideal surface, the next nearest-neighbor peak is also broader and gets closer to the nearest-neighbor peak in superstructures, typically resulting from the next nearest-neighbor water pairs (average distance: 6.55 Å) crossing the defective boundaries, indicated by purple lines in **b**.